Response to Reviewer 2 – Sietske

Manuscript: “Orbital pacing, climate change, and the evolution of Maastrichtian upwelling along the southern Neo-Tethyan margin (Jordan)”

We thank Reviewer 2 for the detailed comments on geological context, GR-record construction, age control, cyclostratigraphic methodology, cycle-thickness variability, the K/Pg hiatus, and the identification and environmental significance of the MME. The revised manuscript now makes these analytical steps and stratigraphic arguments substantially more explicit.

Comment 1

Reviewer comment: Geologic setting
Consider including a paleogeographic map of the Tethyan margin area. Are the 7 wells in figure 1 indicated on the map, and do these include the studied wells

Response: We have added a paleogeographic figure and reorganized the geological-setting figures so that the regional and local contexts of the studied succession are clear. Figure 1 now shows the Maastrichtian paleogeographic setting of the southern Neo-Tethyan margin and the position of central Jordan, together with the regional distribution of the Levant upwelling system. Figure 2 provides the geological map of Jordan and explicitly shows the locations of the studied SA-01 and AJ-02 wells, as well as the additional sections/wells used for regional stratigraphic correlation. We also expanded the accompanying text to distinguish clearly between the two wells from which the new data presented in this study were obtained and the additional wells/sections included only for regional correlation. This revision should remove the ambiguity in the original Figure 1.

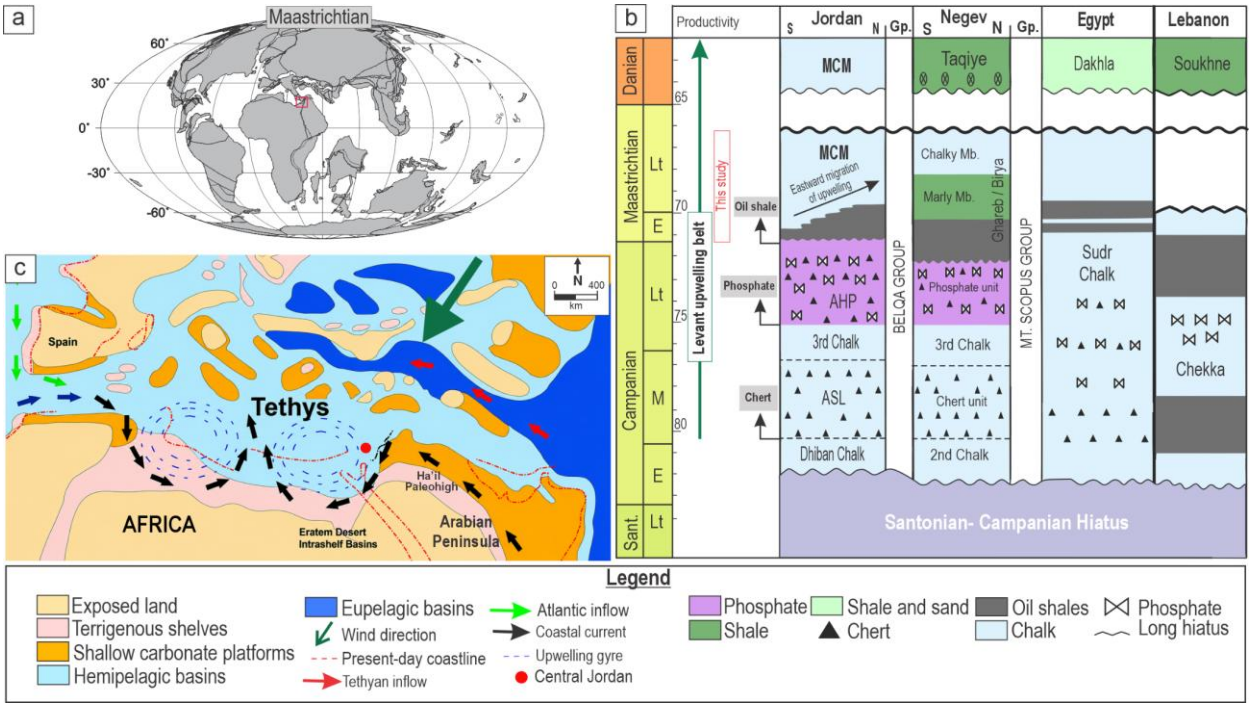


Figure 1. Late Cretaceous paleogeographic and stratigraphic setting of the Levant upwelling system. *(a) Maastrichtian paleogeography and location of central Jordan. (b) Regional stratigraphic correlation across Jordan, Negev, Egypt, and Lebanon, highlighting phosphorite, chert, and organic-rich deposits associated with enhanced productivity (Messaoud et al., 2025). (c) Maastrichtian Tethyan paleogeography showing major*

depositional environments, circulation, prevailing winds, and the Levant upwelling system (Guiraud et al., 2005; MacLeod et al., 2011; Soudry et al., 2006).

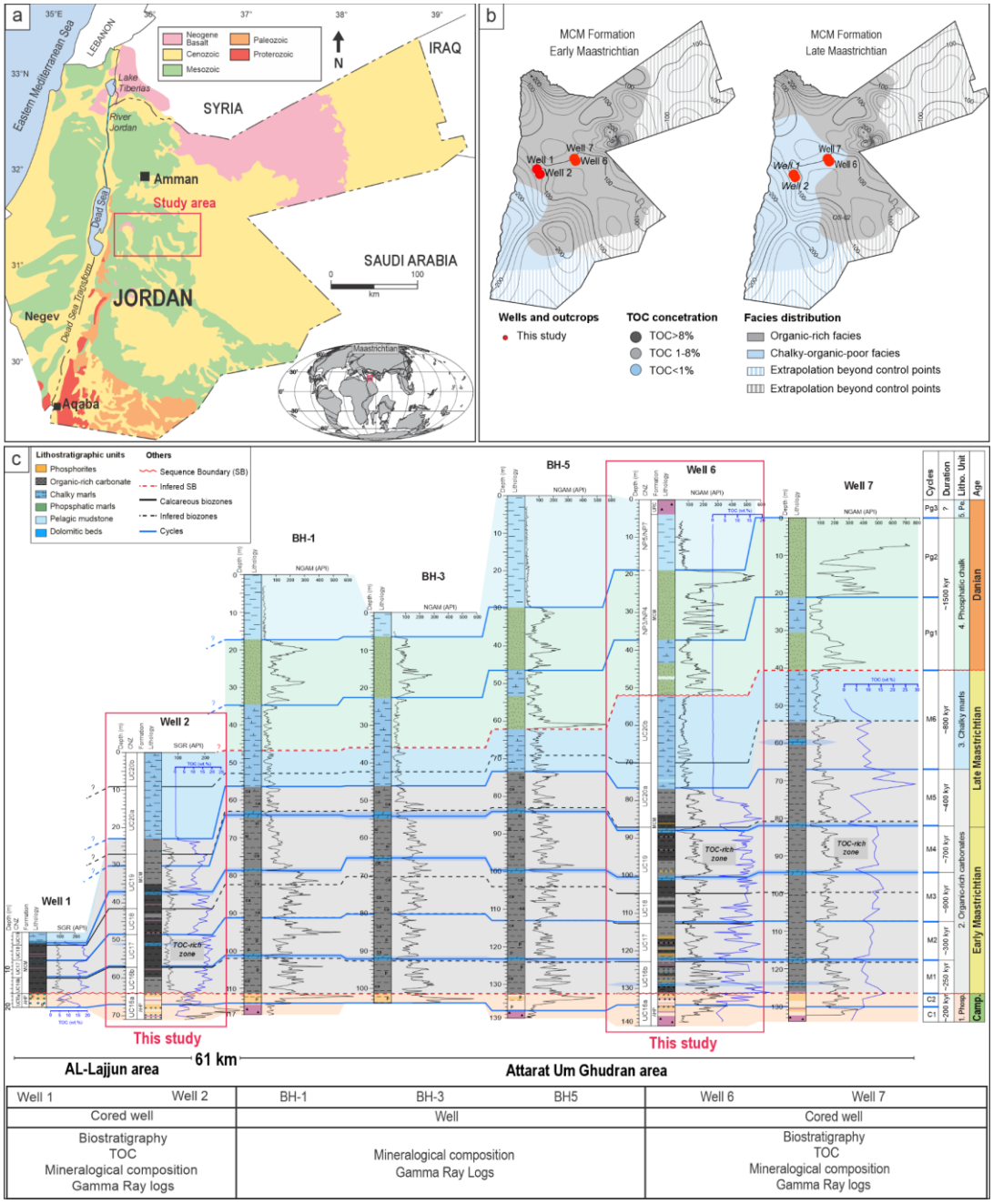


Figure 2. *(a) Geological map of Jordan showing the locations of the studied wells and outcrop (modified from Kalifi et al., 2025). (b) Isopach maps illustrating the spatial distribution of organic-rich facies within the Maastrichtian Muwaqqar Chalk Marl (MCM) Formation (*(Ardila-Sanchez et al., 2026)*). Calcareous nannofossil zonation and biostratigraphic data are compiled from Messaoud et al. (2025), (Alqudah et al., 2015), and (Beik et al., 2019). (c) Regional lithostratigraphic correlation of Maastrichtian sections in central Jordan, flattened at the base of UC16b corresponding to a major gamma-ray peak and phosphorite-rich horizon (Ardila-Sanchez et al., 2026).*

Comment 2

Reviewer comment: Methodology
Please provide more information on how the GR data were collected for the different cores or wells and how they were made into a composite record (Fig. 9).
Include information on how time series analysis was performed, such as the software used and the settings applied. Consider performing time series analyses on the TOC data.
Explain how the tuning was performed.

Response: We thank the reviewer for this helpful comment. The Methods section has been expanded to describe more explicitly the origin and treatment of the GR records, the correlation between the studied wells, and the construction of the record used for cyclostratigraphic analysis. We now distinguish the individual well records from the regional correlation so that the reader can follow which dataset was used for each analysis. We have also added the methodological details required to reproduce the time-series analysis, including the software, preprocessing, spectral method, background-noise model, significance testing, evolutionary/wavelet analysis, filtering, and the parameters used. Following the reviewer's suggestion, spectral analyses were additionally performed on TOC and other independent sedimentological/geochemical proxies. These analyses provide an independent test of the cyclicity observed in the GR record. Finally, the astronomical tuning procedure is now described explicitly. The analysis is presented in its actual sequence: the GR record was first analysed in the untuned depth domain; significant wavelengths and their stratigraphic evolution were then evaluated; the orbital interpretation was assessed against the available independent age constraints and expected orbital hierarchy; and only subsequently was the GR series transformed to the time domain. We have clarified that the untuned depth-domain spectrum provides the primary evidence for the sedimentary cyclicity, whereas the tuned spectrum is used as a consistency check within the astronomical age framework.

Cyclostratigraphic and time-series analyses

Cyclostratigraphic analyses were performed primarily on the high-resolution GR record from Well 6, which provides the most continuous dataset through the studied Maastrichtian succession. Before spectral analysis, the GR record was linearly interpolated to a constant sampling interval and detrended to remove long-term trends while preserving shorter-scale cyclic variability. Dominant spectral components were identified using the Multi-Taper Method (MTM; (Thomson, 1982), with their significance evaluated against an AR(1) red-noise background model. Evolutionary Fast Fourier Transform (evoFFT) analysis was additionally applied to assess changes in spectral power and cycle wavelengths through the succession and to evaluate variations potentially related to changes in sediment accumulation rate (Kodama and Hinnov, 2015). The principal cyclic components were subsequently isolated by band-pass filtering using the Taner filter (Taner, 2000). Time-series analyses were conducted principall using Acycle (Li et al., 2019), complemented by MATLAB-based routines following (Kodama and Hinnov, 2015). To evaluate the reproducibility and robustness of the cyclicity identified in Well 6, additional MTM analyses were performed on independent sedimentary records, including GR from wells well 6 and well 7, TOC from well 6 and well 2, total sulfur from well 2, and $CaCO_3$ from well 6. The occurrence of comparable spectral components across different wells and independent proxies was used to distinguish persistent depositional cyclicity from local or proxy-specific variability and to strengthen the astronomical interpretation. Astronomical calibration was based primarily on the identification of the stable 405-kyr long-eccentricity cycle in the high-resolution Well 6 GR record. The resulting cyclostratigraphic framework was constrained by independent biostratigraphic tie points and used to construct the age model for the Maastrichtian succession. Transformation from the depth to the time domain followed the approach of Kodama and Hinnov (2015).

Comment 3

Reviewer comment: Results
Display the results of the SA-01 core where they are described (before figure 3). Line 254 suddenly mentions cycles, indicate what this refers to. The subscript of figure 2 discusses non displayed items from line 271 onwards.
Consider presenting an age-depth plot for both cores, with all the available age information,

including the biostratigraphic datums, d13C events and the cyclostratigraphic tuning.
Section 4.7 might be better suited for the discussion, and the authors should discuss how the position of the K/Pg boundary is inferred, or whether there is a hiatus. Discuss whether you think that the entire record is (biostratigraphically) complete.
Provide data tables.

Response: We thank the reviewer for these suggestions. We have reorganized the Results so that the SA-01 core description and associated data are presented before they are interpreted or compared with AJ-02. The previously abrupt reference to “cycles” has been rewritten so that the term is introduced and defined before use, and the caption of the relevant figure has been revised to describe only information that is actually displayed. We have also added age-depth models for both studied cores, incorporating the available biostratigraphic age constraints and showing the principal intervals of stratigraphic condensation.

The relationship between these independent age constraints and the cyclostratigraphic framework is now explained in the text. The K/Pg interval has been expanded substantially. In SA-01, the uppermost Cretaceous samples contain a late Maastrichtian assemblage assigned to the upper UC20b Subzone. Above this interval, the assemblage changes abruptly: characteristic Maastrichtian taxa disappear and the first clearly identified Paleogene assemblage is attributable to NP3 near the 53 m level. The intervening UC20c-UC20d and NP1-NP2 assemblages are not recorded. Assignment to NP3 is supported by the occurrence of ***Chiasmolithus danic***us, whose lowest occurrence defines the base of NP3. We therefore infer a substantial hiatus encompassing the latest Maastrichtian, the K/Pg boundary, and part of the early Danian. Comparable K/Pg hiatuses in central Jordan have previously been reported by Alqudah et al. (2015), Farouk et al. (2014), and Giraldo-Gómez et al. (2018). Section 4.7 has also been reorganized so that descriptive correlation remains in the Results, while the broader paleoenvironmental interpretation has been moved to the Discussion. The requested numerical data tables are provided as supplementary Excel files.

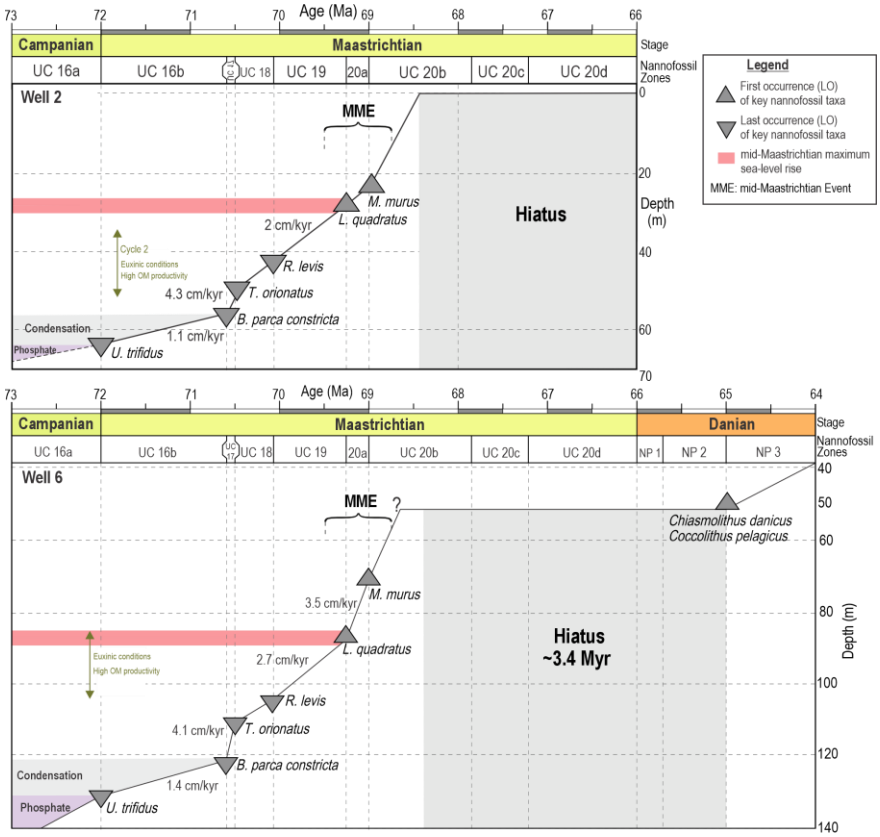


Figure 10. Age–depth models for Wells 2 (top) and 6 (bottom), constrained by selected calcareous nannofossil bioevents. Sedimentation rates are indicated along the age–depth curves. Pink shading marks the mid-Maastrichtian maximum sea-level rise, whereas grey areas indicate stratigraphic hiatuses. Condensed phosphatic intervals and associated euxinic, high-productivity conditions are also shown.

Comment 4

Reviewer comment: Cyclostratigraphy:

Discuss if there is a rhythmic alternation of lithologies and whether this is reflected in the GR record. The text mentions an estimated sedimentation rate, please explain how this rate was obtained. The GR series is tuned, but any information on how this was done is lacking. The MTM spectrum of the tuned GR series looks less convincing than the spectral analysis in the depth domain. The colourmap of the wavelet does not allow identification of dominant periodicities.
Some observations on the variations in the GR data: Prominent peaks around 80 m follow a longer periodicity in the depth domain than peaks around 130 m, yet all are interpreted as short eccentricity (figure 12). They may be driven by other periodicities, or there might be changes in sedimentation rate.

Response: We thank the reviewer for these important observations. We agree that the original manuscript did not sufficiently explain the relationship between lithological cyclicity and the GR signal, the derivation of sedimentation rates, the tuning procedure, or the observed changes in cycle thickness. We have therefore substantially revised the cyclostratigraphic Methods, Results, and figures.

The Maastrichtian succession shows recurrent lithological and compositional variations that are reflected in the GR record. The organic-rich interval consists predominantly of bituminous and chalky marls, with variations in carbonate, organic matter, and siliciclastic content, together with subordinate dolomitic and phosphatic horizons. These changes generate corresponding GR variability. However, because GR responds to multiple sedimentary components, we do not associate individual GR peaks with a single lithology. Instead, GR is treated as a continuous proxy for compositional variability. Comparable cyclic patterns in TOC, carbonate, sulfur, and organic-matter records further support a depositional origin for the observed GR cyclicity.

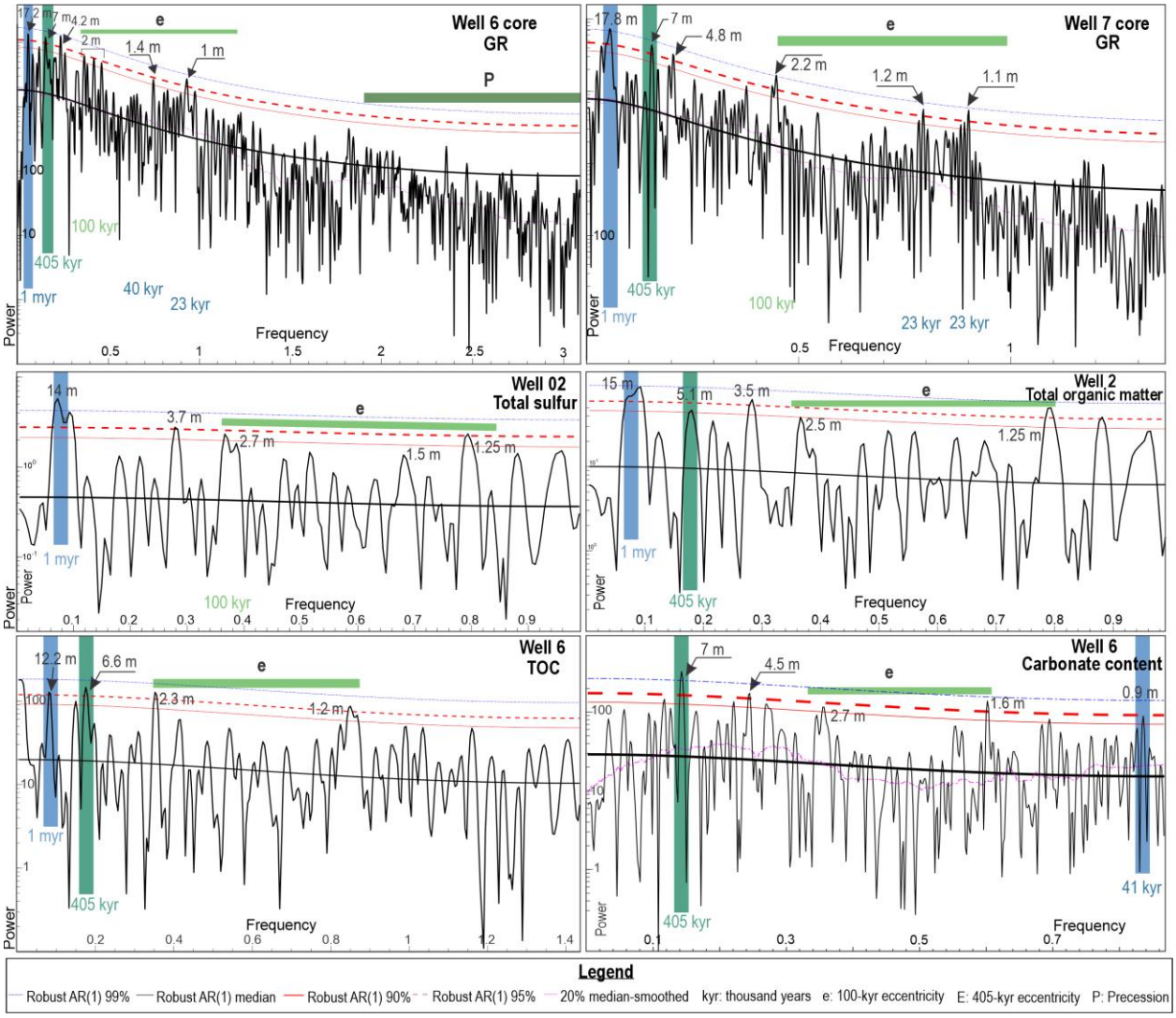


Figure 12. *MTM spectral analysis of Maastrichtian sedimentological and geochemical records showing the expression of orbital-scale cyclicity across independent proxies. Blue shading marks the 405 kyr long-eccentricity range, green shading the ~100 kyr short-eccentricity range, and the higher-frequency bands correspond to precession-scale variability. Confidence levels are shown by the robust AR(1) thresholds and median/background-noise estimates.*

We have also clarified the derivation of sedimentation rates. Rather than assuming a constant rate, the revised analysis reconstructs stratigraphic changes in accumulation rate. Rates are approximately 3 cm kyr^{-1} between 139–128 m, decrease to ~1.8–2.0 cm kyr^{-1} between 128–110 m, increase to ~4.2 cm kyr^{-1} around 106 m, and subsequently decrease upward to ~2.1–2.3 cm kyr^{-1}. The methodology and these variations are now explicitly presented in the revised manuscript and figures.

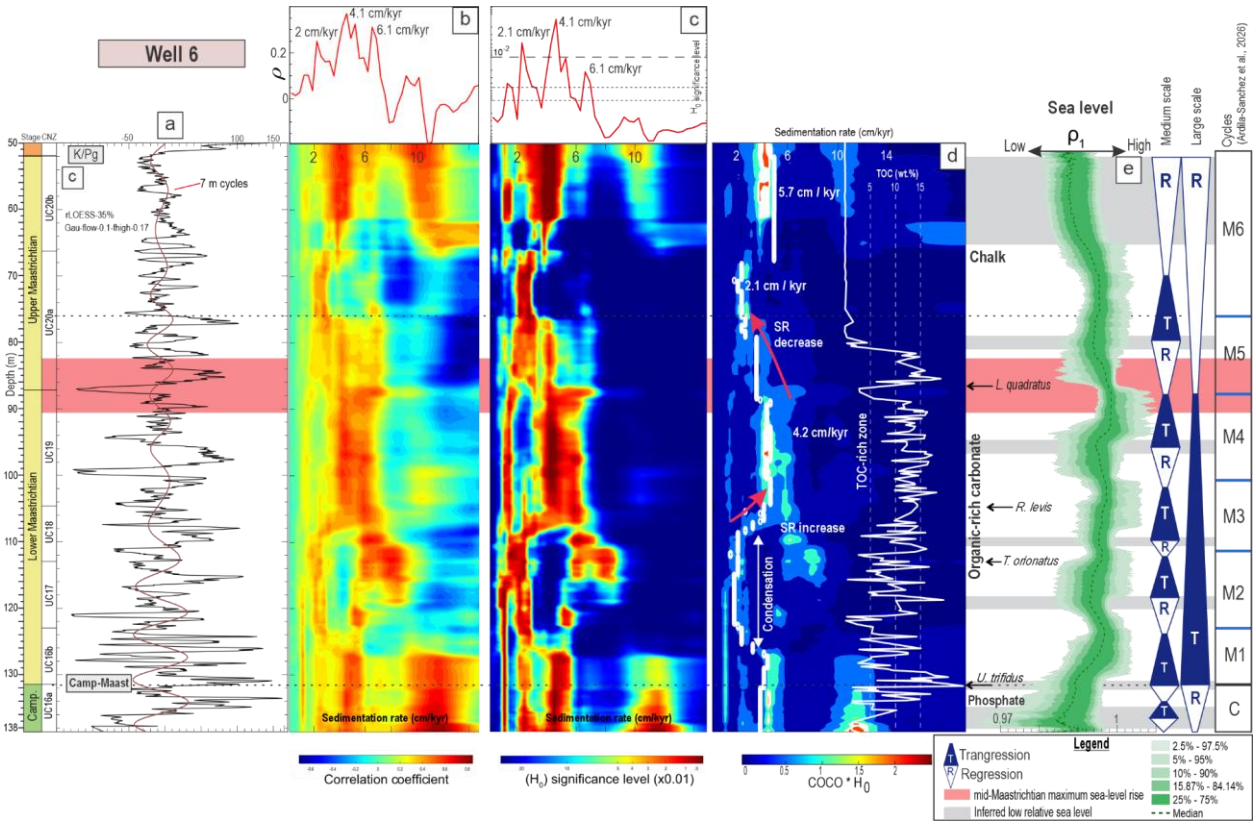


Figure 13. *S*edimentation-rate evolution and sequence-stratigraphic organization of the Maastrichtian succession in Well 6. (a) GR record and filtered orbital component. (b–c) eCOCO and sedimentary-noise analyses showing changes in sedimentation rate through the succession. (d) Sedimentation-rate evolution compared with TOC, highlighting intervals of condensation and shifts in accumulation rate. (e) Sequence-stratigraphic interpretation showing relative sea-level change, transgressive–regressive cycles, key nannofossil bioevents, and depositional facies. The red interval marks the mid-Maastrichtian maximum sea-level rise.

The astronomical tuning procedure is now described step by step. Cyclostratigraphic analysis was first conducted on the untuned GR record in the depth domain using MTM and evolutionary/wavelet analyses. Significant wavelengths and their stratigraphic evolution were then evaluated against the expected orbital hierarchy and independent age constraints before conversion to the time domain. We agree that the depth-domain spectrum provides the stronger evidence and therefore now present it as the primary cyclostratigraphic result. The spectrum of the tuned series is retained only as a consistency check.

The wavelet figure has also been revised with a clearer colour scale and explicit indication of the main wavelength bands, allowing changes in dominant periodicities and cycle thickness to be more readily identified.

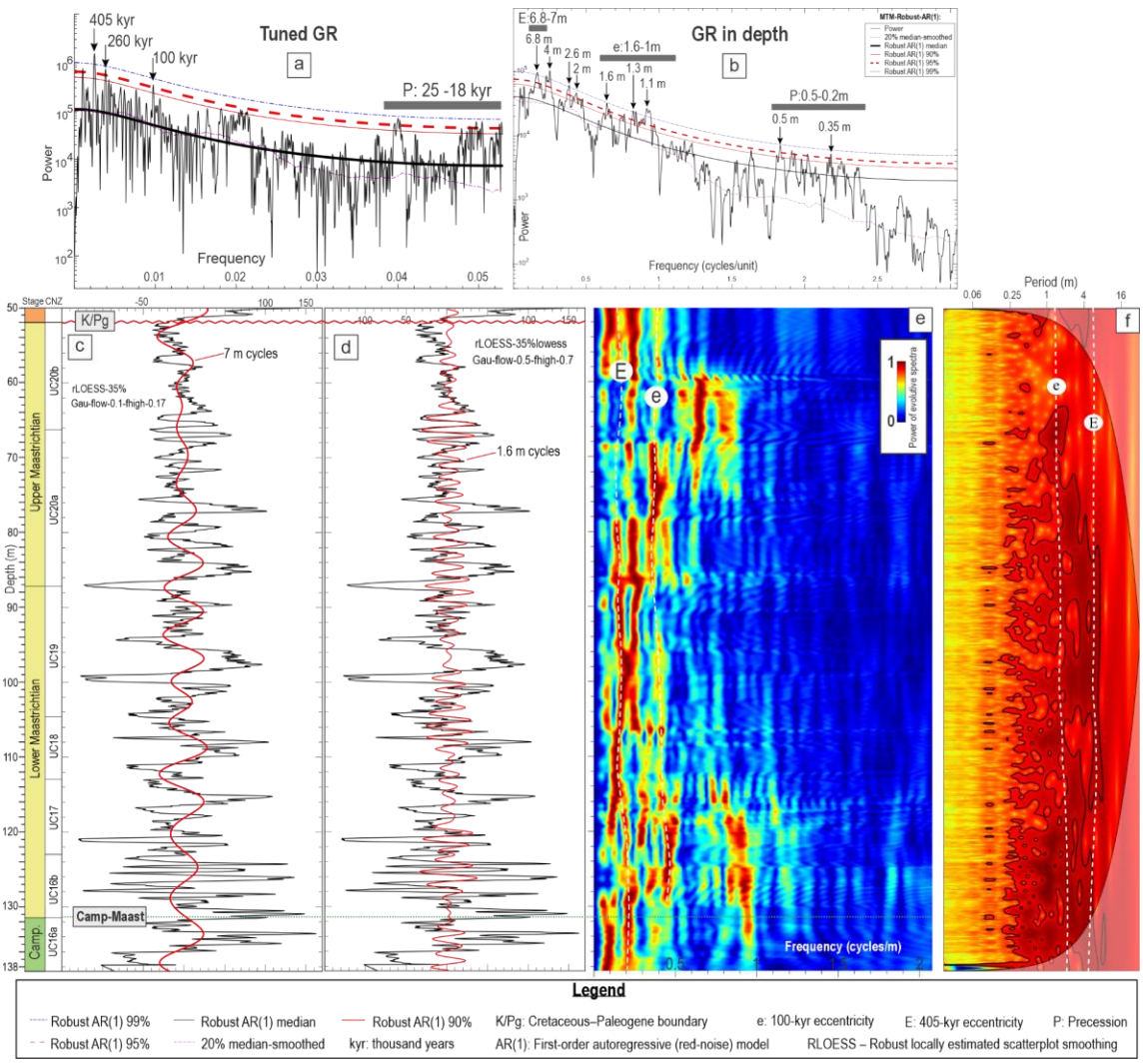


Figure 11. *Cyclostratigraphic analysis of the Maastrichtian gamma-ray (GR) record from Well 6.* ***(a)*** *MTM power spectrum of the astronomically tuned GR series, highlighting spectral peaks corresponding to the 405-kyr and ~100-kyr eccentricity and precession (~25–18 kyr) bands.* ***(b)*** *MTM spectrum of the untuned GR record in the depth domain, showing significant sedimentary wavelengths associated with the main orbital bands.* ***(c)*** *Stratigraphic framework and filtered long-eccentricity (405-kyr) component used for astronomical tuning.* ***(d)*** *Original GR record plotted against depth.* ***(e)*** *Evolutive harmonic analysis (EHA) showing changes in spectral power and the persistence of eccentricity-related frequencies through the succession.* ***(f)*** *Wavelet power spectrum illustrating the depth-dependent distribution of orbital cyclicity; dashed lines indicate the expected eccentricity bands and the curved boundary marks the cone of influence.*

Finally, we agree with the reviewer that the different spacing of GR peaks around ~80 m and ~130 m should not automatically be interpreted as the same short-eccentricity cycle. Much of this difference can be explained by changing sedimentation rates: for example, a 100-kyr cycle would correspond to ~2 m at 2 cm kyr^{-1} but ~4 m at 4 cm kyr^{-1}. We have therefore adopted a more conservative interpretation and no longer assign individual GR peaks to short eccentricity based solely on their spacing. Orbital interpretations are instead based on the overall spectral hierarchy, changes in spectral power, reconstructed sedimentation rates, independent age constraints, and comparison with other sedimentological and geochemical proxies.

Comment 5

Reviewer comment: Discussion

The identification of the mid Maastrichtian event is critical for this paper, yet not an easy feat and the main figure (10) can be improved. Why are there two panels, and why does the d13C curve of Gubbio look different in the two panels?

Section 5.5 has a lot of paleoenvironmental mechanisms, but these are not clearly linked to the own data.

Response: We thank the reviewer for these important comments. We agree that identification of the mid-Maastrichtian Event (MME) is central to the manuscript and that the original figure did not present the correlation sufficiently clearly. The original two-panel design of Figure 10 was intended to show the Jordan record at different levels of detail, but we agree that it introduced unnecessary redundancy and made the Gubbio $\delta^{13}C$ reference curve appear inconsistent. We have therefore replaced this presentation with a single, internally consistent correlation panel using the same Gubbio dataset and scaling throughout. The revised figure emphasizes the diagnostic carbon-isotope features together with the independent calcareous nannofossil bioevents that constrain their stratigraphic positions.

The identification of the MME is now explained more explicitly in the text. It is based on the combined expression of the M1+, M1−, M2+, M2−, and M3+ carbon-isotope features and is independently constrained by the succession of nannofossil bioevents, including Uniplanarius trifidus, Broinsonia parca constricta, Tranolithus orionatus, Reinhardtites levis, Micula praemurus, and Lithraphidites quadratus. We have also clearly distinguished the broader ~69.5-67.5 Ma mid-Maastrichtian climatic perturbation from the shorter ~570 kyr MME sensu stricto following Dubicka et al. (2024).

This makes the criteria used to identify and position the event in Jordan explicit rather than relying on visual similarity between $\delta^{13}C$ curves alone. We also agree that the previous version of Section 5.5 invoked several paleoenvironmental mechanisms without linking each of them sufficiently closely to our own observations.

The section has therefore been substantially reorganized around the measured datasets. Changes in the upwelling system are now discussed directly in relation to: (i) GR and TOC cyclicity; (ii) the transition from organic-rich to carbonate-rich facies; (iii) the decline of cool-water nannofossil taxa and increase in Watznaueria; (iv) the $\delta^{18}O$ trend; (v) variations in detrital proxies such as Al_2O_3 and Ti; (vi) the reconstructed sedimentation-rate evolution; and (vii) the independently developed sequence-stratigraphic/relative sea-level framework.

We have also separated observations from mechanisms more clearly and softened interpretations that cannot be demonstrated directly by the Jordanian data. Orbital forcing is now presented as a mechanism that may have modulated seasonal insolation, atmospheric circulation, regional winds, and hydroclimate, whereas the primary evidence is the observed hierarchy and recurrence of cyclicity in GR, TOC, and other proxies. Similarly, sea level is treated principally as a control on accommodation, shelf geometry, and the spatial position of the upwelling-productivity system rather than as a direct cause of stronger upwelling. Finally, the interpretation of environmental change across the MME is now anchored directly to the Jordanian observations. The interval is associated with the decline of organic-rich sedimentation, expansion of carbonate-rich facies, decreasing cool-water nannofossil taxa, increasing Watznaueria, and $\delta^{18}O$ changes consistent with warming. These observations support our interpretation of a reorganization and migration of the upwelling system during the mid-Maastrichtian, rather than a simple direct weakening of upwelling caused by warming.

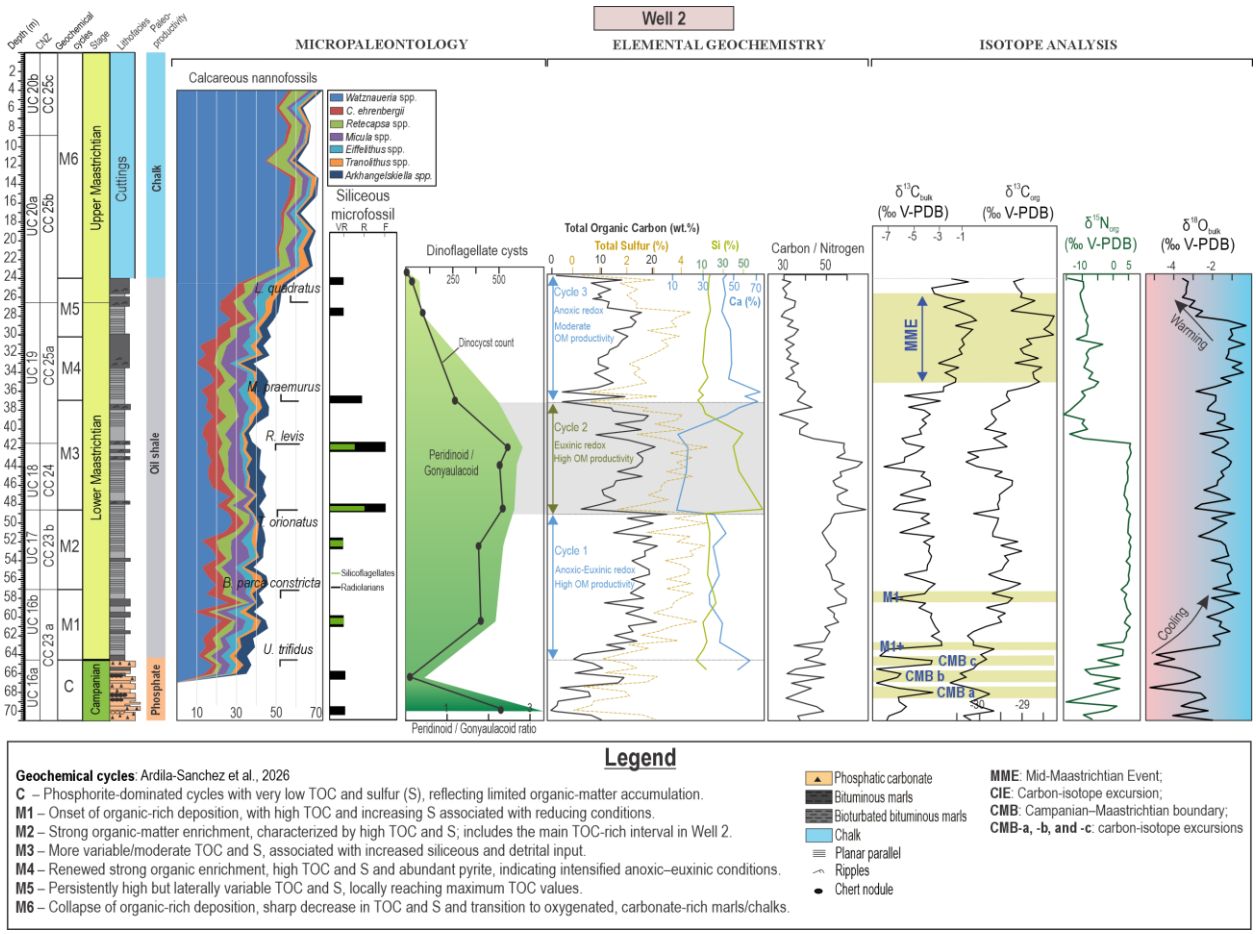


Figure 4. Integrated stratigraphic, micropaleontological, geochemical, and paleoenvironmental framework of Well 2 (upper Campanian–upper Maastrichtian). Three depositional cycles record shifts from phosphogenic upwelling and organic-matter enrichment to oligotrophic carbonate production, alongside the CMBE and MME

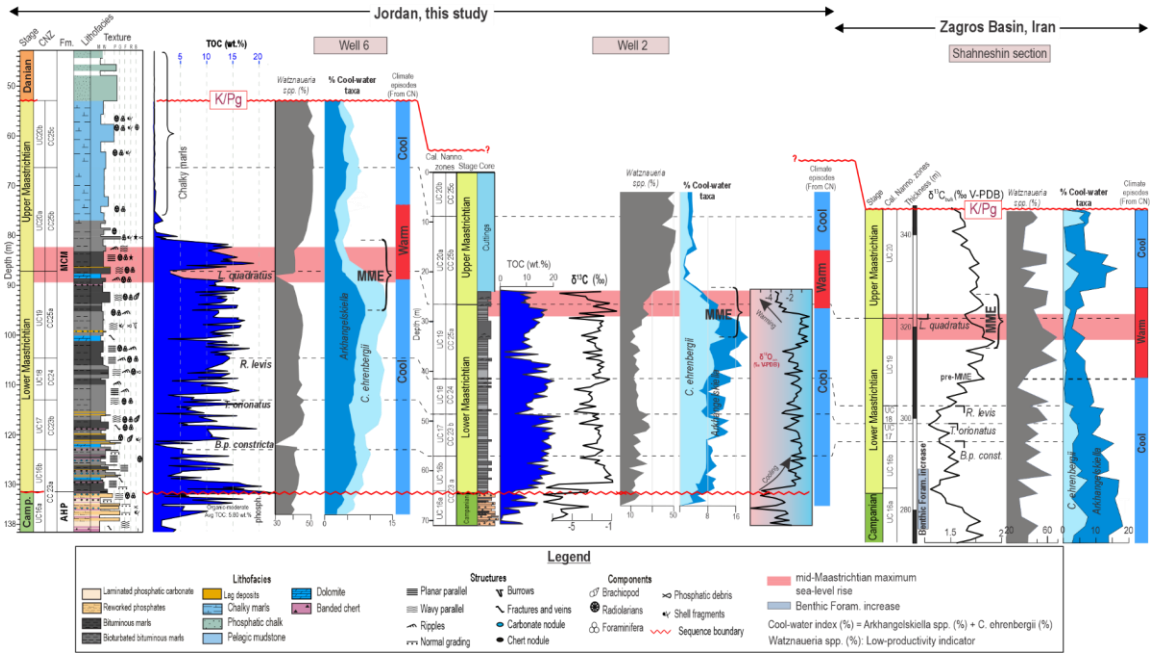


Figure 9. Integrated stratigraphic, geochemical, and paleoclimatic correlation of the upper Campanian–Maastrichtian to lower Danian succession from Wells 6 and 2 (Jordan) and the Shahneshin section (Zagros Basin, Iran). Records include lithostratigraphy, GR, TOC, calcareous nannofossil assemblages, cool-water index, and $\delta^{18}O$. Dashed lines mark key biostratigraphic correlations, the blue interval highlights the mid-Maastrichtian maximum transgression and MME, and red wavy lines indicate major stratigraphic boundaries, including the K/Pg boundary.

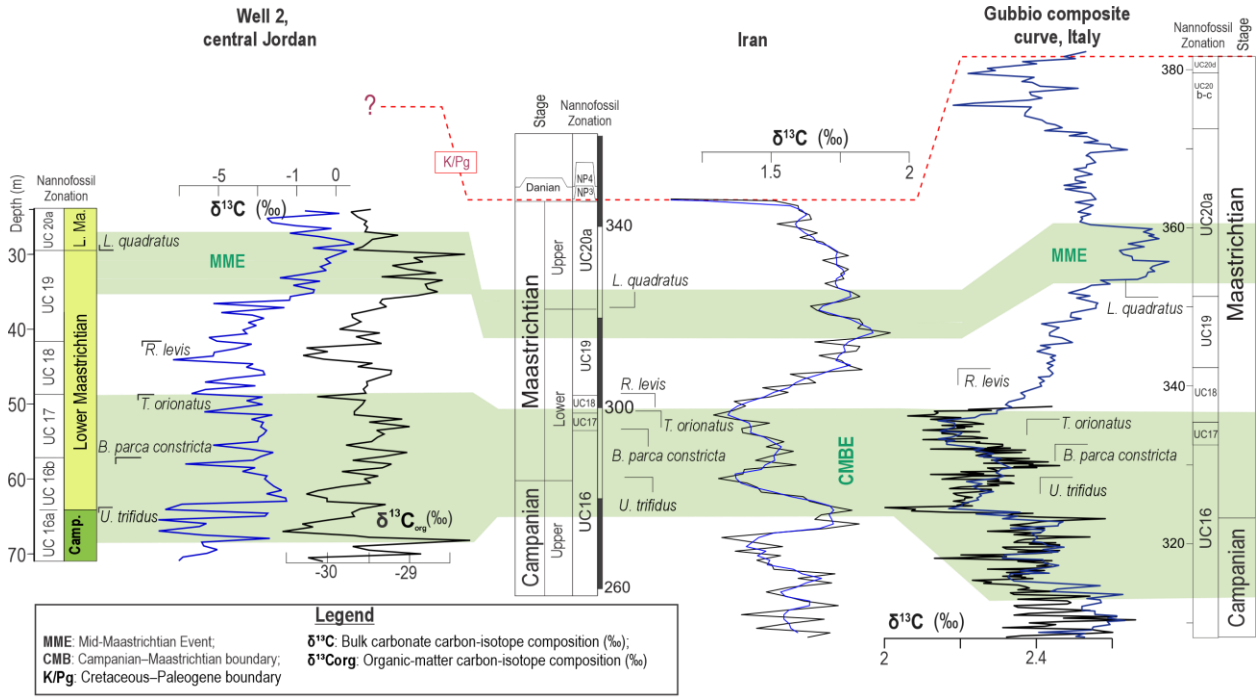


Figure 14. Carbon-isotope stratigraphic correlation of Well 2 (central Jordan) with the Shahneshin section, Iran (Razmjooei et al., 2020), and the Gubbio composite curve, Italy. $\delta^{13}C$ records and key calcareous nannofossil bioevents constrain the correlations across the Campanian–Maastrichtian interval. Green shading highlights the correlated carbon-isotope excursions, including the Campanian–Maastrichtian Boundary Event (CMBE) and Mid-Maastrichtian Event (MME). The red dashed line indicates the inferred correlation toward the K/Pg boundary.

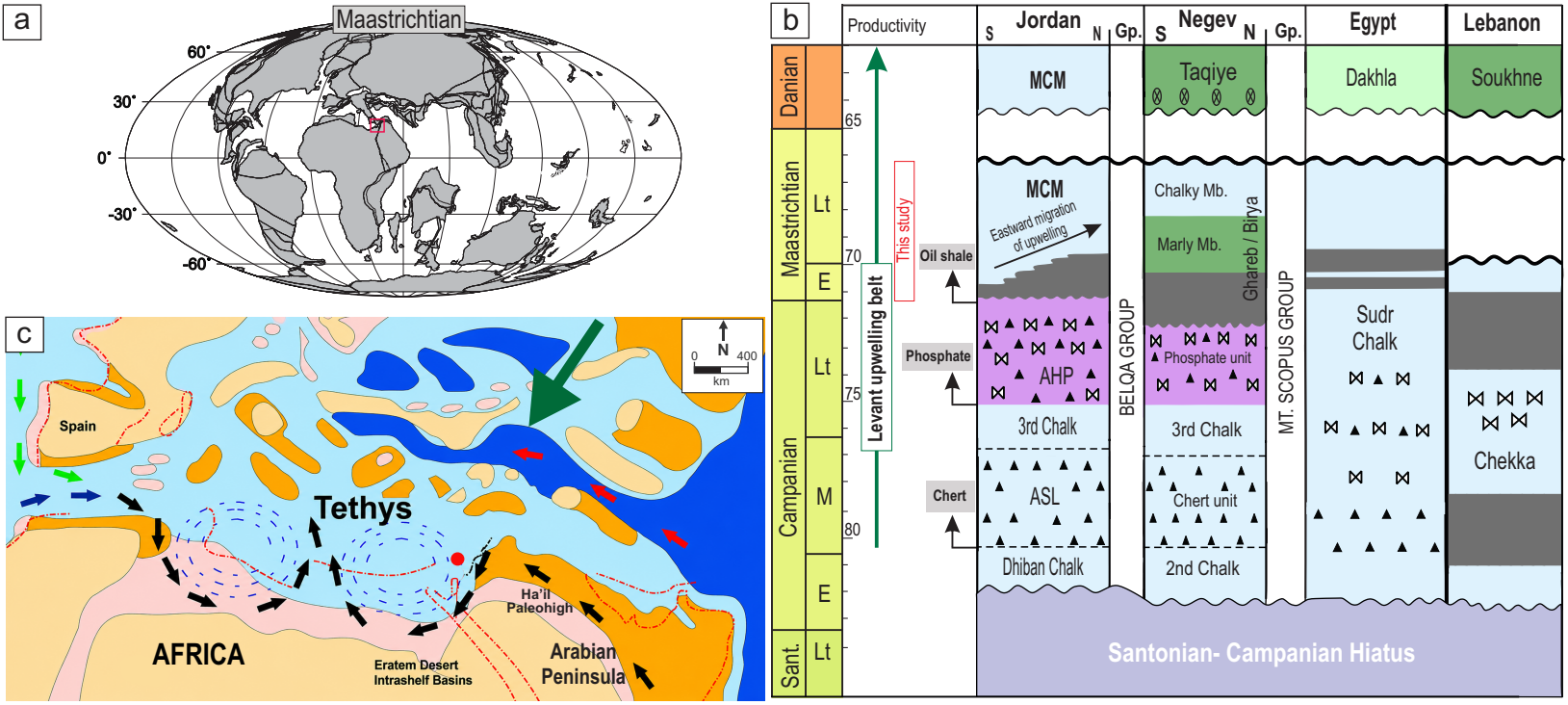
References cited in the response

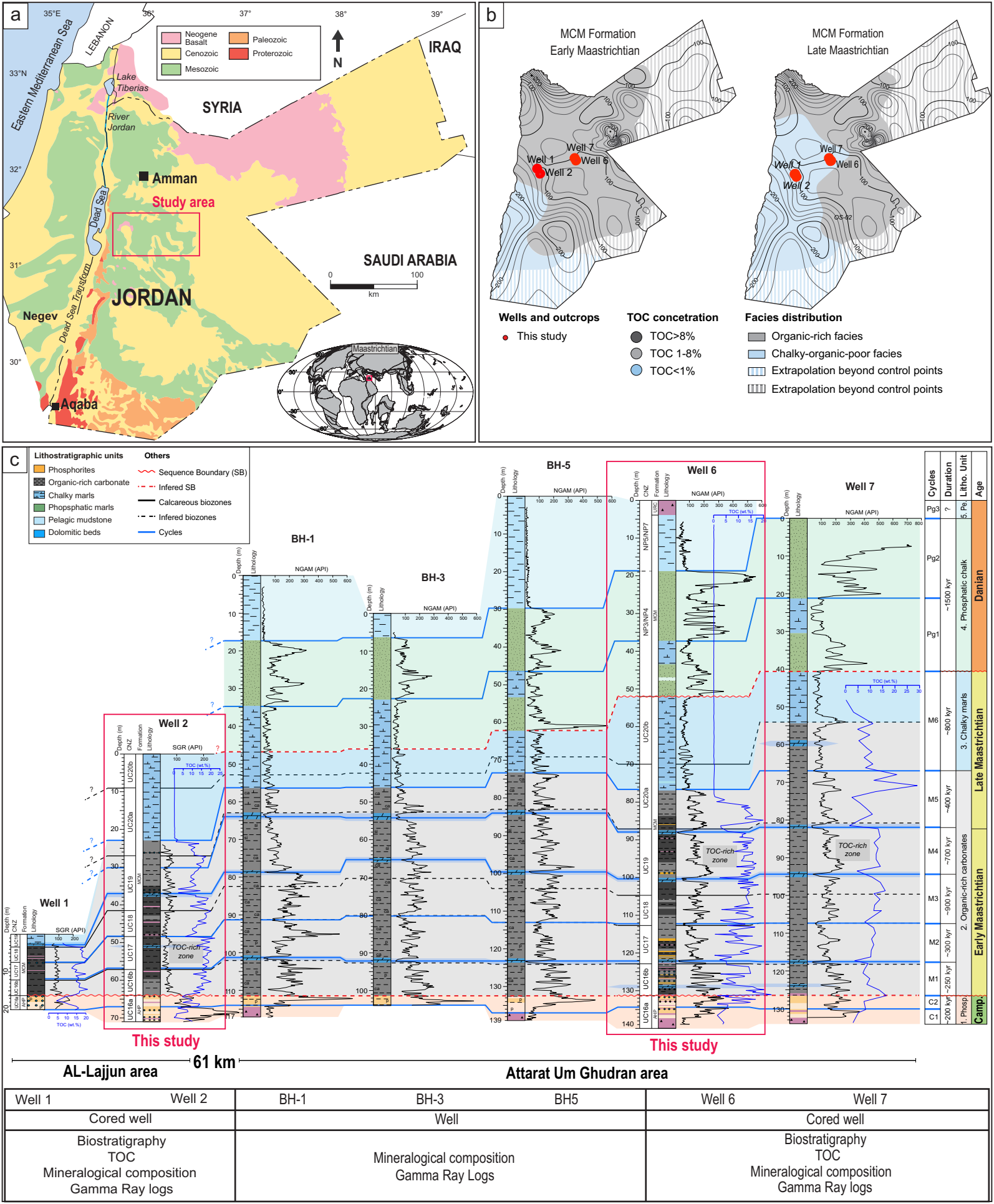
Alqudah, M., Ali Hussein, M., van den Boorn, S., Podlaha, O. G., and Mutterlose, J. (2015). Biostratigraphy and depositional setting of Maastrichtian–Eocene oil shales from Jordan. Marine and Petroleum Geology, 60, 87–104.

Farouk, S., Marzouk, A. M., and Ahmad, F. (2014). The Cretaceous/Paleogene boundary in Jordan. Journal of Asian Earth Sciences, 94, 113–125.

Giraldo-Gómez, V. M., Beik, I., Podlaha, O. G., and Mutterlose, J. (2018). A paleoenvironmental analysis of benthic foraminifera from Upper Cretaceous–lower Paleocene oil shales of Jordan. Cretaceous Research, 91, 1–13.

Dubicka, Z., Wierny, W., Bojanowski, M. J., Rakociński, M., Walaszczyk, I., and Thibault, N. (2024). Multi-proxy record of the mid-Maastrichtian event in the European Chalk Sea: Paleoceanographic implications. Gondwana Research, 129, 1–22.


a
Maastrichtian
60°
30°
0°
-30°
-60°
b
Productivity
S
Jordan
N
Gp.
S
Negev
N
Gp.
Egypt
Lebanon
Danian
Maastrichtian
Lt
E
Campanian
Lt
M
E
Sant.
Lt
65
70
75
80
Levant upwelling belt
This study
Oil shale
Phosphate
Chert
MCM
Eastward migration of upwelling
AHP
3rd Chalk
ASL
Dhiban Chalk
BELQA GROUP
Taqiye
Chalky Mb.
Marly Mb.
Ghareb / Birya
Phosphate unit
3rd Chalk
Chert unit
2nd Chalk
MT. SCOPUS GROUP
Dakhla
Sudr Chalk
Soukhne
Chekka
Santonian- Campanian Hiatus
c
N
0
400
km
Spain
Tethys
AFRICA
Ha'il Paleohigh
Arabian Peninsula
Eratem Desert Intrashelf Basins
Legend
Exposed land
Terrigenous shelves
Shallow carbonate platforms
Hemipelagic basins
Eupelagic basins
Wind direction
Present-day coastline
Tethyan inflow
Atlantic inflow
Coastal current
Upwelling gyre
Central Jordan
Phosphate
Shale
Shale and sand
Chert
Oil shales
Chalk
Phosphate
Long hiatus



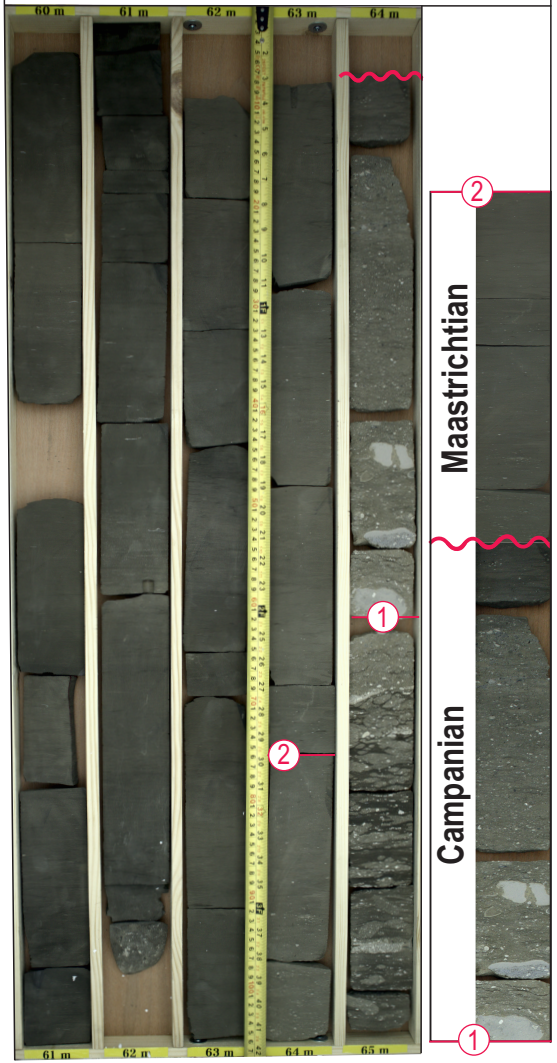
Well 1	Well 2	BH-1	BH-3	BH5	Well 6	Well 7
Cored well		Well			Cored well	
Biostratigraphy TOC Mineralogical composition Gamma Ray logs		Mineralogical composition Gamma Ray Logs			Biostratigraphy TOC Mineralogical composition Gamma Ray logs	

AJ-02

Phosphatic interval (Late Campanian): 72 m to 64.6 m

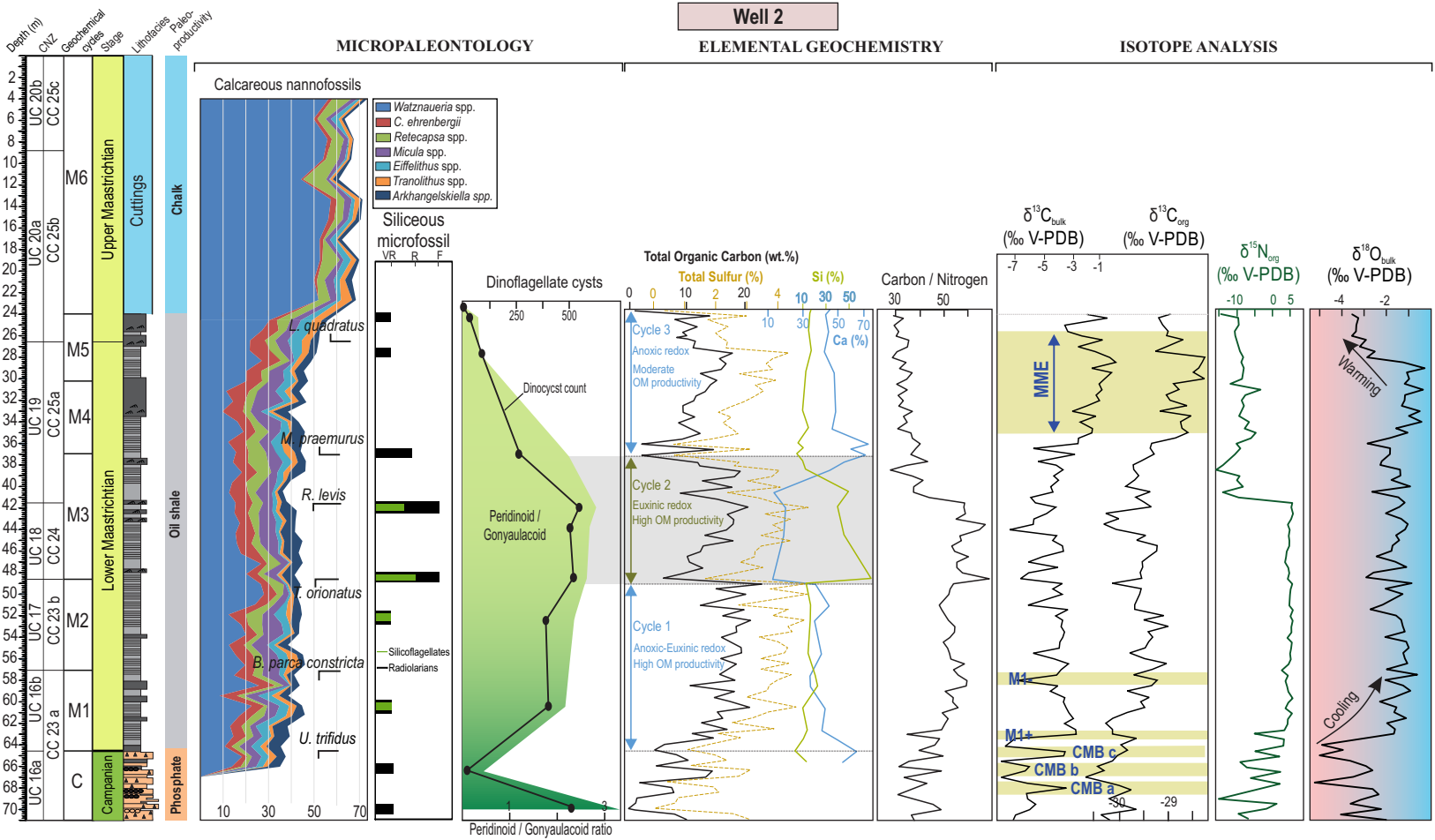


Campanian - Maastrichtian boundary (at the AHP-MCM boundary)



Early Maastrichtian Oil shale interval: 64.4 m to 24 m





Legend

Geochemical cycles: Ardila-Sanchez et al., 2026

C – Phosphorite-dominated cycles with very low TOC and sulfur (S), reflecting limited organic-matter accumulation.

M1 – Onset of organic-rich deposition, with high TOC and increasing S associated with reducing conditions.

M2 – Strong organic-matter enrichment, characterized by high TOC and S; includes the main TOC-rich interval in Well 2.

M3 – More variable/moderate TOC and S, associated with increased siliceous and detrital input.

M4 – Renewed strong organic enrichment, high TOC and S and abundant pyrite, indicating intensified anoxic–euxinic conditions.

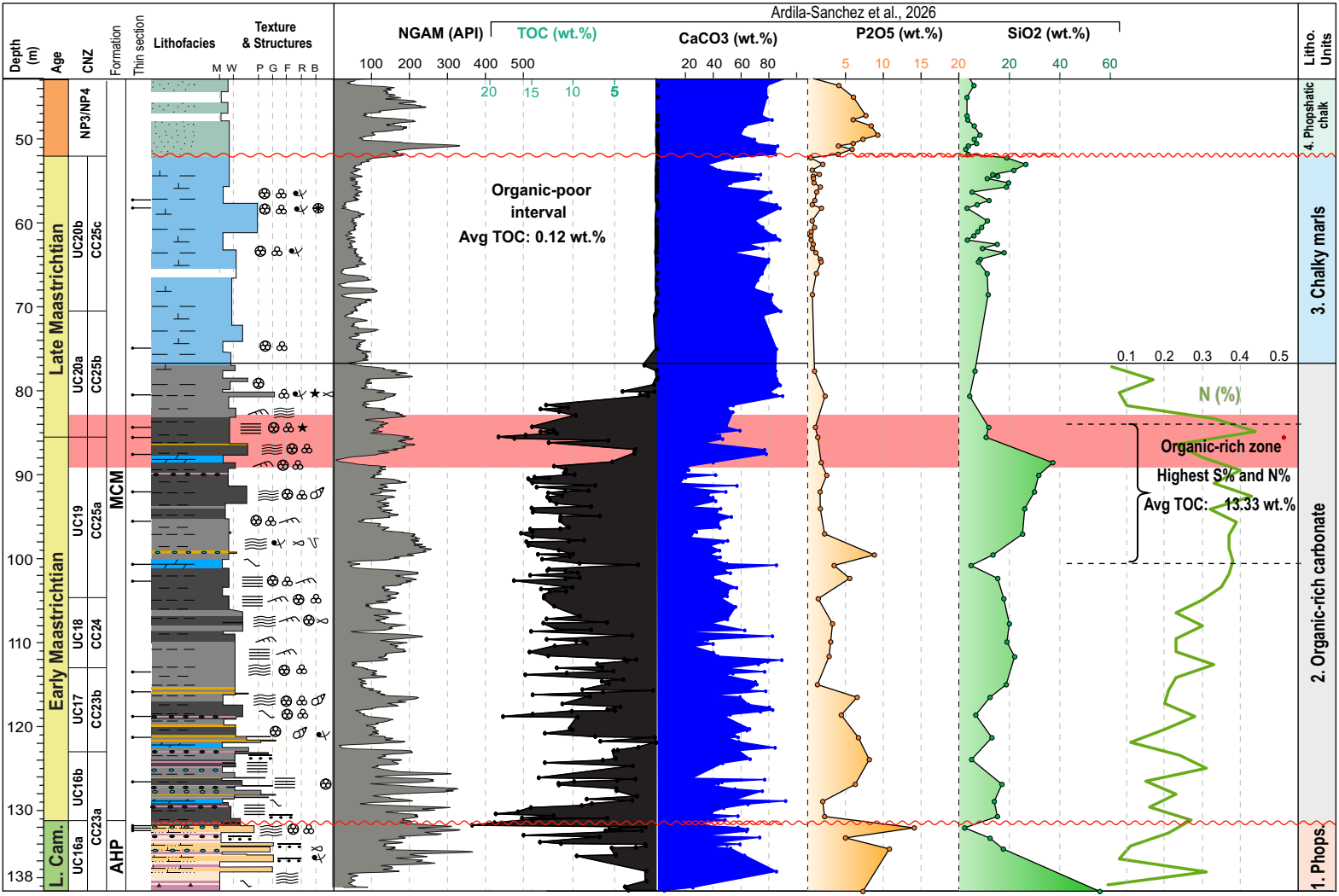
M5 – Persistently high but laterally variable TOC and S, locally reaching maximum TOC values.

M6 – Collapse of organic-rich deposition, sharp decrease in TOC and S and transition to oxygenated, carbonate-rich marls/chalks.

- Phosphatic carbonate
- Bituminous marls
- Bioturbated bituminous marls
- Chalk
- Planar parallel
- Ripples
- Chert nodule

MME: Mid-Maastrichtian Event;
CIE: Carbon-isotope excursion;
CMB: Campanian–Maastrichtian boundary;
CMB-a, -b, and -c: carbon-isotope excursions

Well 6



Lithofacies

- Laminated phosphatic carbonate
- Reworked phosphates
- Bituminous marls
- Bioturbated bituminous marls
- Phosphatic chalk
- Pelagic mudstone
- Lag deposits
- Chalky marls
- Dolomite
- Banded chert

Structures

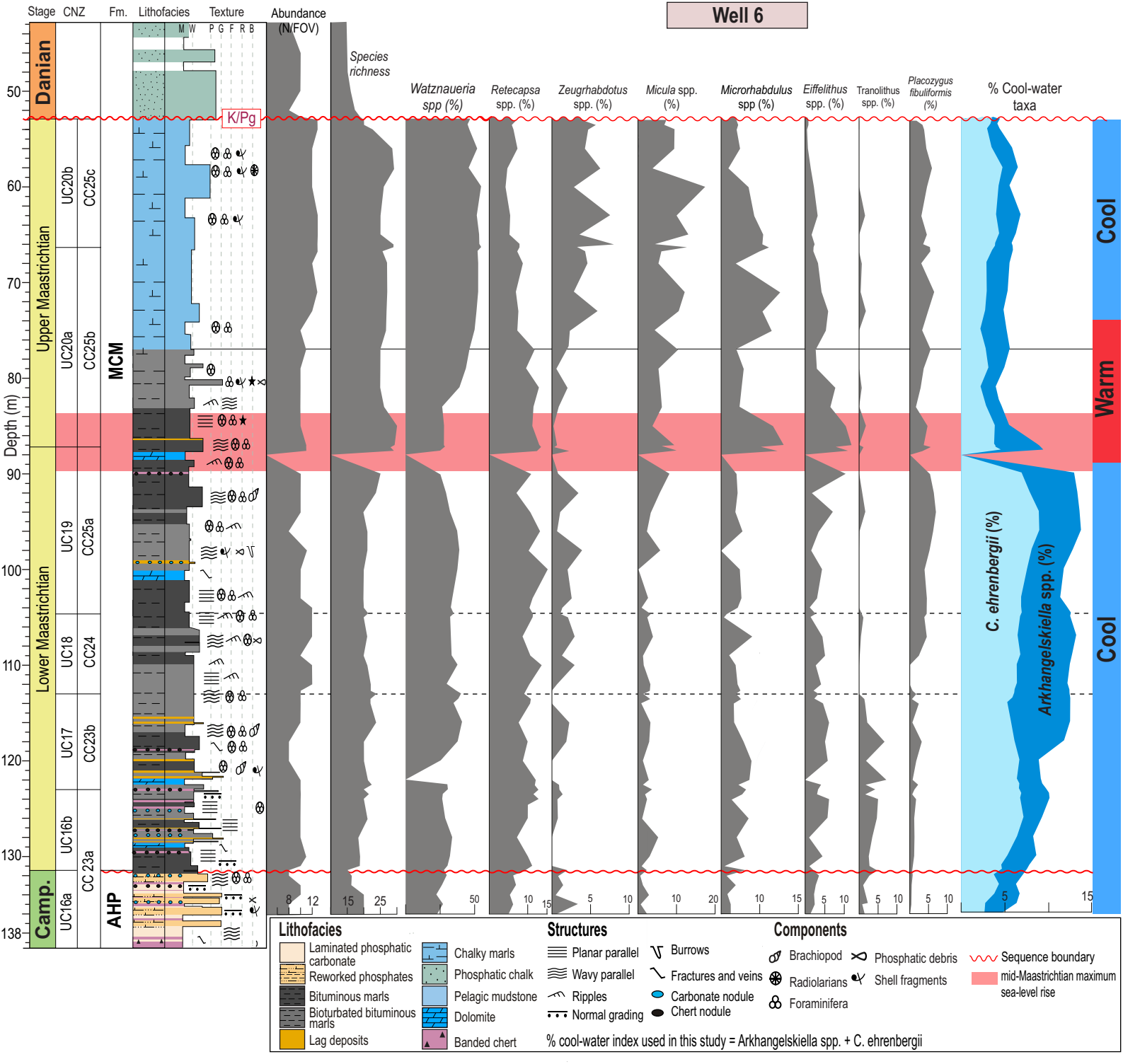
- Planar parallel
- Wavy parallel
- Ripples
- Normal grading
- Burrows
- Fractures and veins

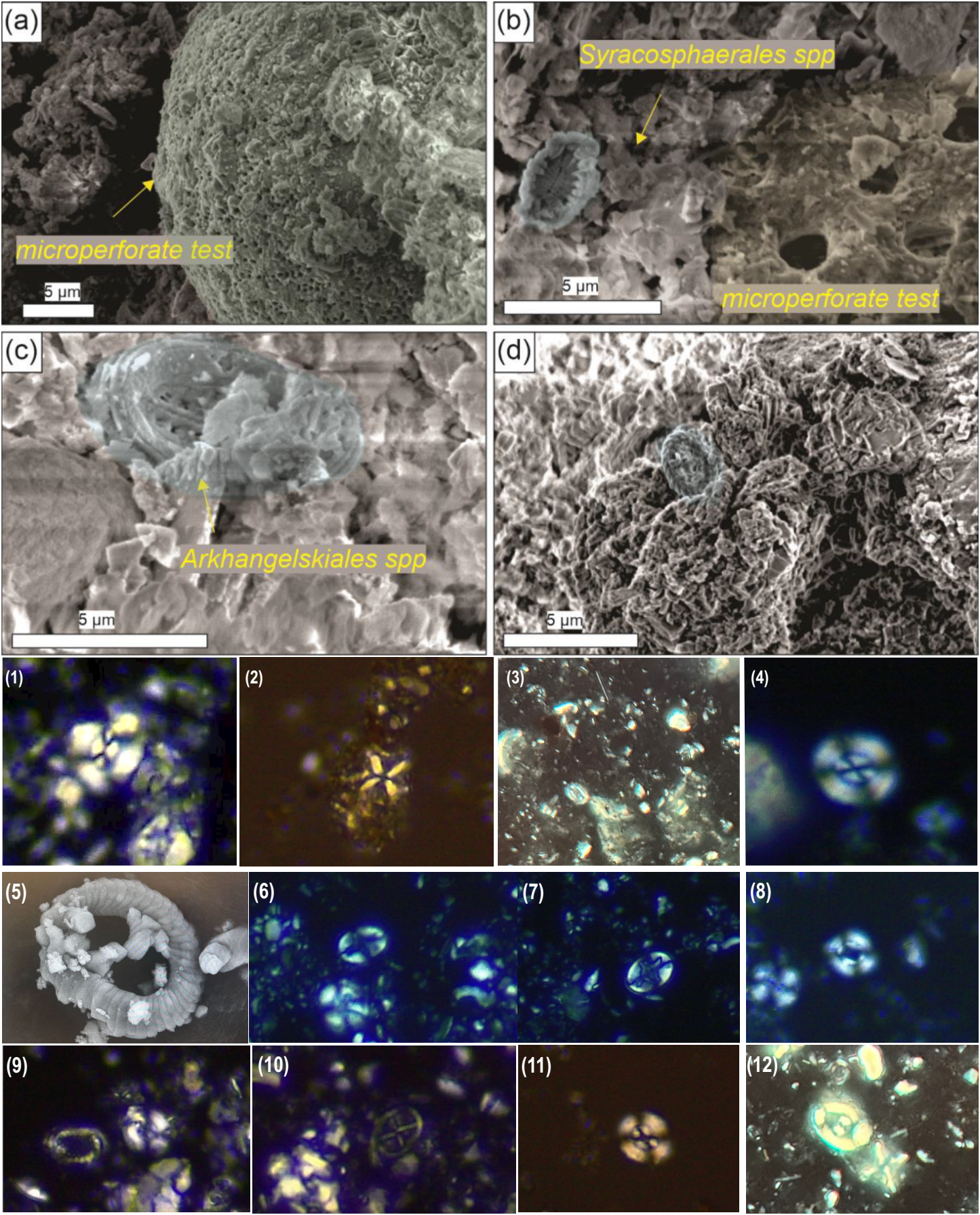
Components

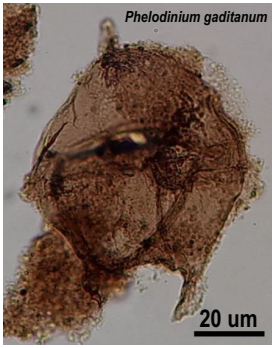
- Carbonate nodule
- Chert nodule
- Brachiopod
- Radiolarians
- Foraminifera
- Phosphatic debris
- Shell fragments

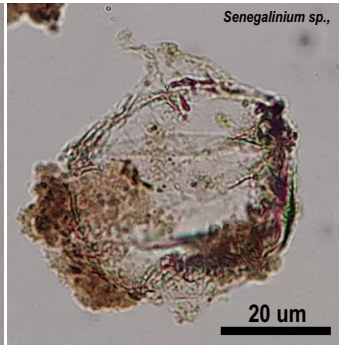
Others

- mid-Maastrichtian maximum sea-level rise
- Sequence boundary

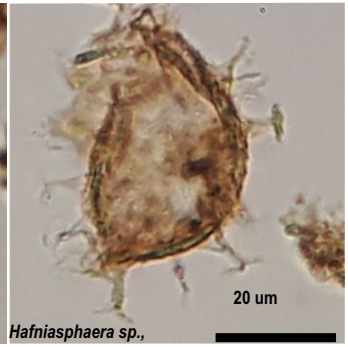

Well 6
Stage
CNZ
Fm.
Lithofacies
Texture
M W P G F R B
Abundance (N/FOV)
Species richness
Watznaueria spp (%)
Retecapsa spp. (%)
Zeugrhabdotus spp. (%)
Micula spp. (%)
Microrhabdulus spp (%)
Eiffelithus spp. (%)
Tranolithus spp. (%)
Placozygus fibuliformis (%)
% Cool-water taxa
Depth (m)
Danian
Upper Maastrichtian
Lower Maastrichtian
Camp.
UC16a
UC16b
UC17
UC18
UC19
UC20a
UC20b
CC 23a
CC23b
CC24
CC25a
CC25b
CC25c
MCM
AHP
K/Pg
Cool
Warm
Cool
C. ehrenbergii (%)
Arkhangelskiella spp. (%)
Lithofacies
Laminated phosphatic carbonate
Reworked phosphates
Bituminous marls
Bioturbated bituminous marls
Lag deposits
Chalky marls
Phosphatic chalk
Pelagic mudstone
Dolomite
Banded chert
Structures
Planar parallel
Wavy parallel
Ripples
Normal grading
Burrows
Fractures and veins
Carbonate nodule
Chert nodule
Components
Brachiopod
Radiolarians
Foraminifera
Phosphatic debris
Shell fragments
Sequence boundary
mid-Maastrichtian maximum sea-level rise
% cool-water index used in this study = Arkhangelskiella spp. + C. ehrenbergii

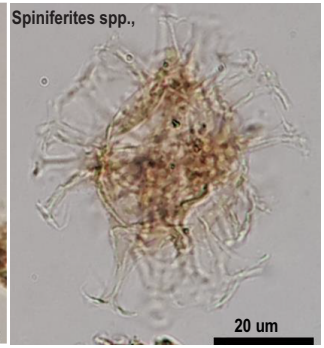

(a)
microperforate test
5 µm
(b)
Syracosphaerales spp
5 µm
microperforate test
(c)
Arkhangelskiales spp
5 µm
(d)
5 µm
(1)
(2)
(3)
(4)
(5)
(6)
(7)
(8)
(9)
(10)
(11)
(12)


Phelodinium gaditanum
20 um


Senegalinium sp.,
20 um

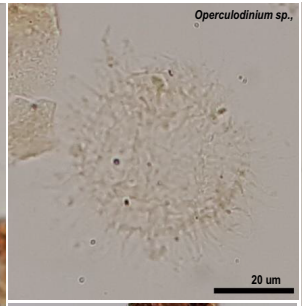

Vozzhennikovia sp.,
20 um


Hafniasphaera sp.,
20 um


Spiniferites spp.,
20 um

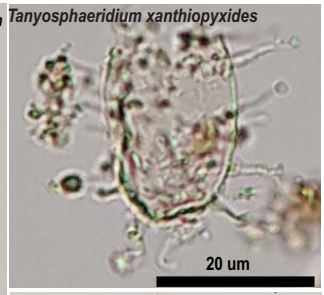

Vozzhennikovia sp.,
20 um


Palaeocystodinium golzowense
20 um

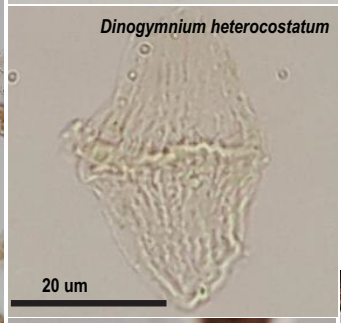

Operculodinium sp.,
20 um


Andalusiella mauthei
20 um

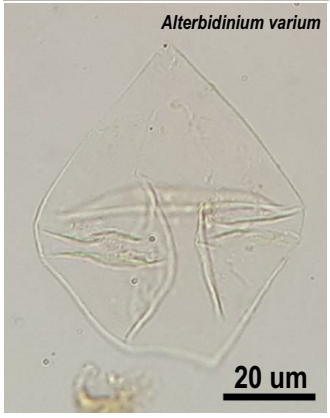

Amphorosphaeridium fenestratum
20 um

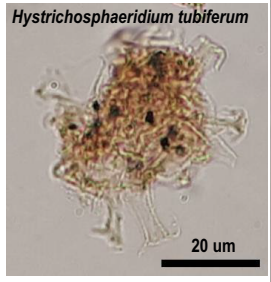

Tanyosphaeridium xanthiopyxides
20 um

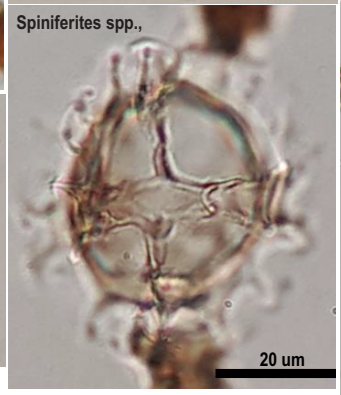

Senegalinium macrocystum
20 um

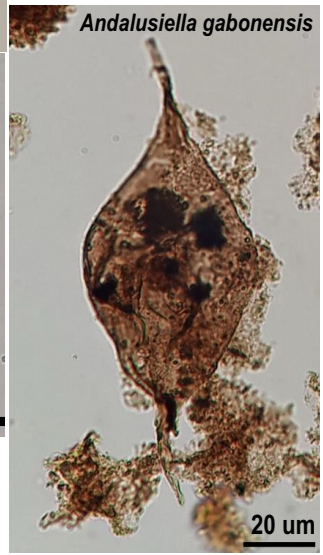

Dinogymnium heterocostatum
20 um

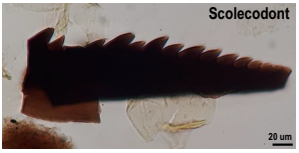

Cerodinium striatum
20 um

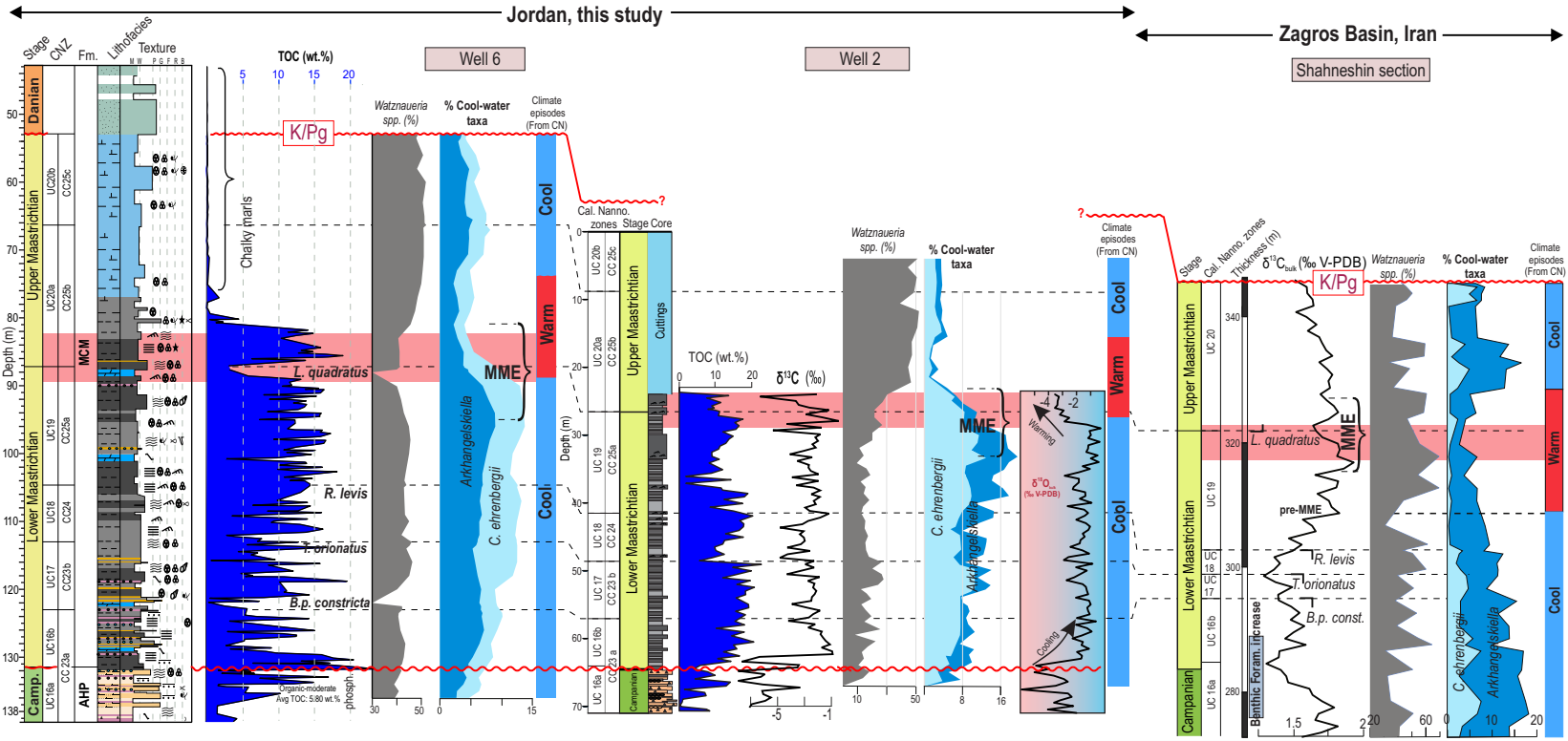

Alterbidinium varium
20 um

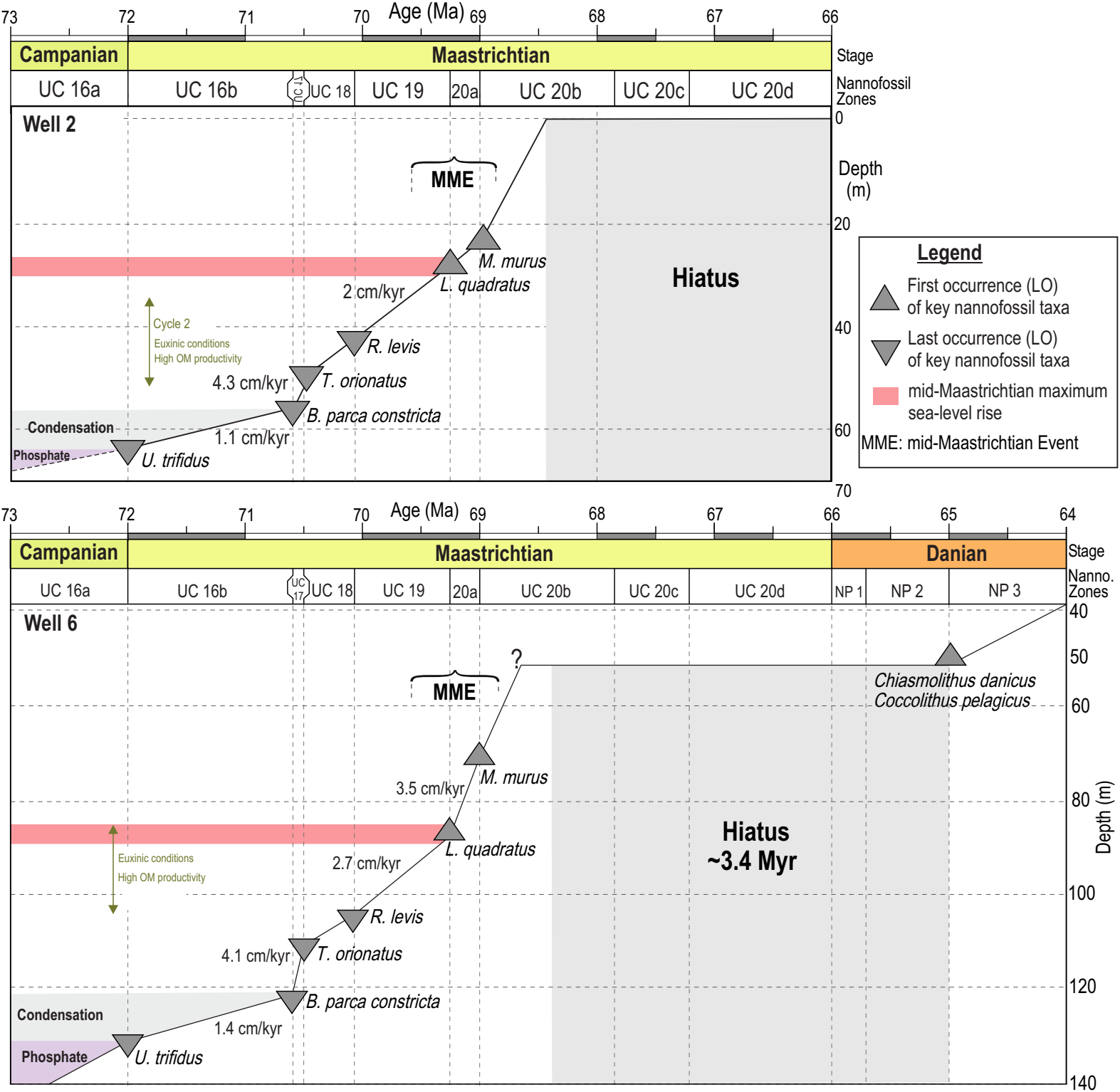

Hystrichosphaeridium tubiferum
20 um

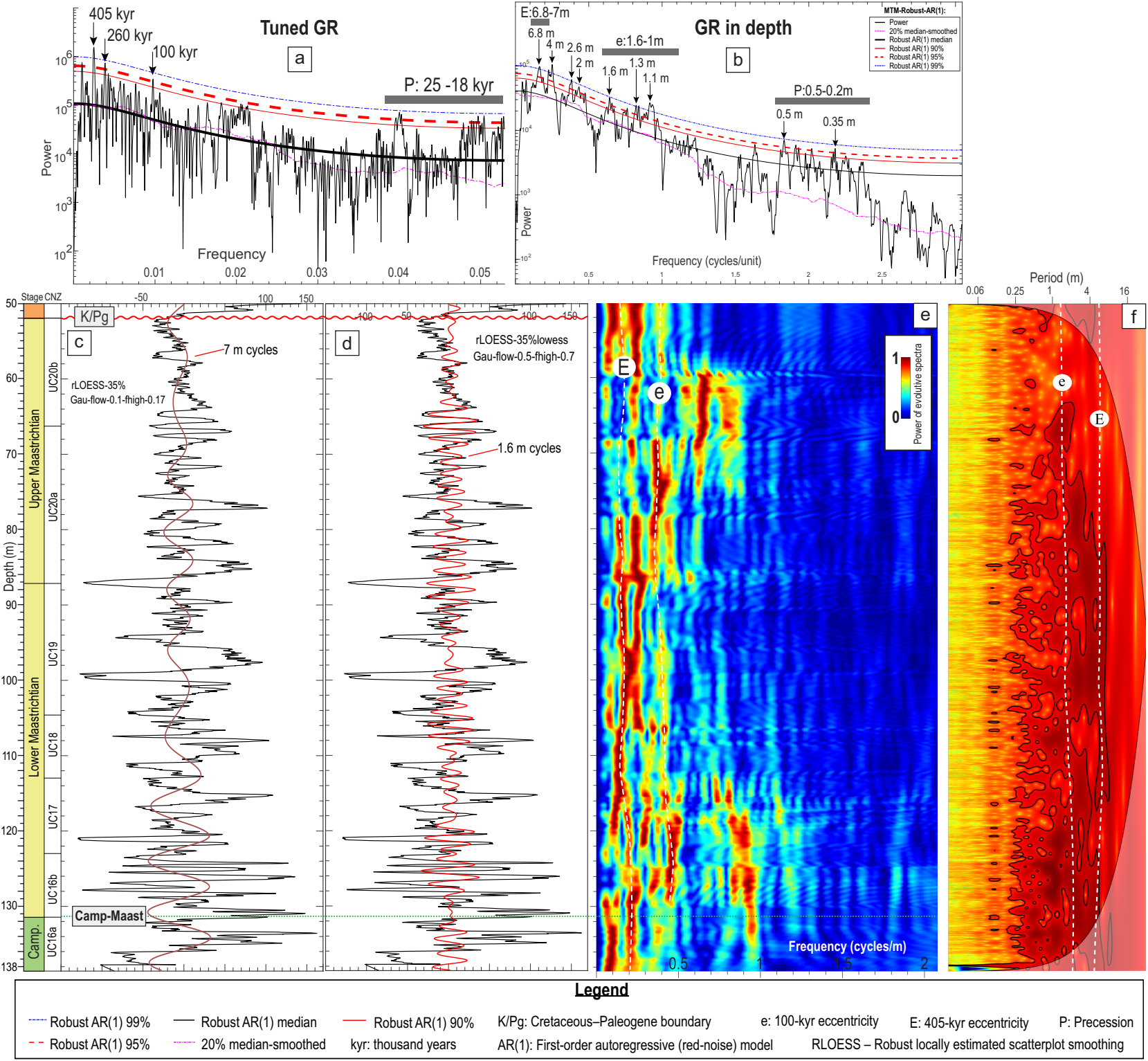

Spiniferites spp.,
20 um


Andalusiella gabonensis
20 um


Scolecodont
20 um


Jordan, this study
Zagros Basin, Iran
Shahneshin section
Well 6
Well 2
Stage
CNZ
Fm.
Lithofacies
Texture
Depth (m)
Danian
Upper Maastrichtian
Lower Maastrichtian
Camp.
MCM
AHP
K/Pg
TOC (wt.%)
Chalky marls
L. quadratus
R. levis
T. orionatus
B.p. constricta
Organic-moderate
Avg TOC: 5.80 wt.%
phosph.
Watznaueria spp. (%)
% Cool-water taxa
Arkhangelskiella
C. ehrenbergii
MME
Climate episodes (From CN)
Cool
Warm
Cool
Cal. Nanno. zones
Stage
Core
Cuttings
Upper Maastrichtian
Lower Maastrichtian
Campanian
δ13C (‰)
δ18O (‰ V-PDB)
Warming
Cooling
Cool
Warm
Cool
Thickness (m)
δ13Cbulk (‰ V-PDB)
pre-MME
B.p. const.
Benthic Foram. increase
Legend
Lithofacies
Laminated phosphatic carbonate
Reworked phosphates
Bituminous marls
Bioturbated bituminous marls
Lag deposits
Chalky marls
Phosphatic chalk
Pelagic mudstone
Dolomite
Banded chert
Structures
Planar parallel
Wavy parallel
Ripples
Normal grading
Burrows
Fractures and veins
Carbonate nodule
Chert nodule
Components
Brachiopod
Radiolarians
Foraminifera
Phosphatic debris
Shell fragments
Sequence boundary
mid-Maastrichtian maximum sea-level rise
Benthic Foram. increase
Cool-water index (%) = Arkhangelskiella spp. (%) + C. ehrenbergii (%)
Watznaueria spp. (%): Low-productivity indicator

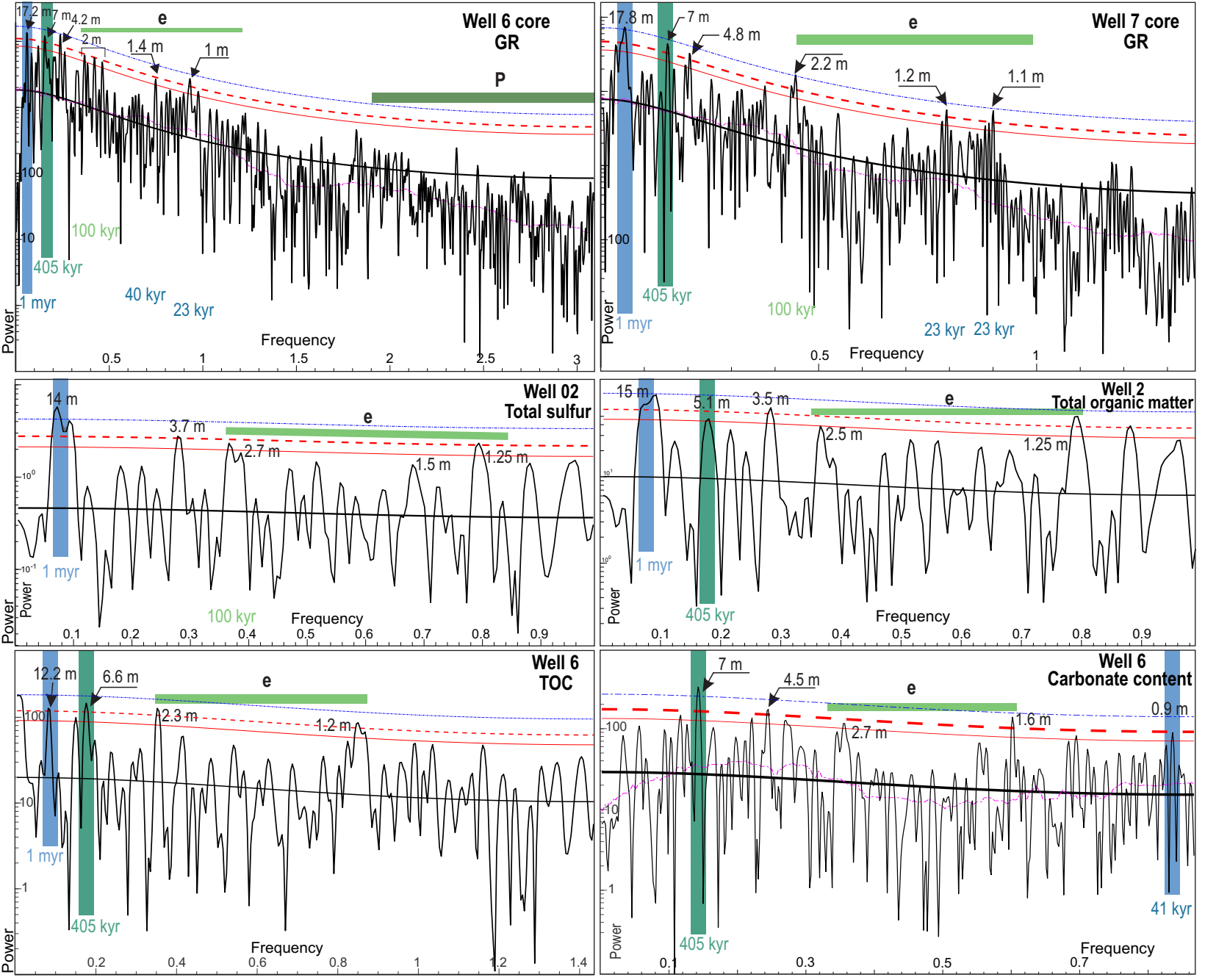

Age (Ma)
73
72
71
70
69
68
67
66
Campanian
Maastrichtian
Stage
UC 16a
UC 16b
UC 17
UC 18
UC 19
20a
UC 20b
UC 20c
UC 20d
Nannofossil Zones
Well 2
MME
Depth (m)
0
20
40
60
70
M. murus
L. quadratus
2 cm/kyr
Hiatus
Cycle 2
Euxinic conditions
High OM productivity
R. levis
4.3 cm/kyr
T. orionatus
B. parca constricta
Condensation
1.1 cm/kyr
Phosphate
U. trifidus
Legend
First occurrence (LO) of key nannofossil taxa
Last occurrence (LO) of key nannofossil taxa
mid-Maastrichtian maximum sea-level rise
MME: mid-Maastrichtian Event
Age (Ma)
73
72
71
70
69
68
67
66
65
64
Campanian
Maastrichtian
Danian
Stage
UC 16a
UC 16b
UC 17
UC 18
UC 19
20a
UC 20b
UC 20c
UC 20d
NP 1
NP 2
NP 3
Nanno. Zones
Well 6
?
MME
Chiasmolithus danicus
Coccolithus pelagicus
40
50
60
80
100
120
140
Depth (m)
M. murus
3.5 cm/kyr
L. quadratus
2.7 cm/kyr
Hiatus
~3.4 Myr
Euxinic conditions
High OM productivity
R. levis
4.1 cm/kyr
T. orionatus
B. parca constricta
Condensation
1.4 cm/kyr
Phosphate
U. trifidus



Legend

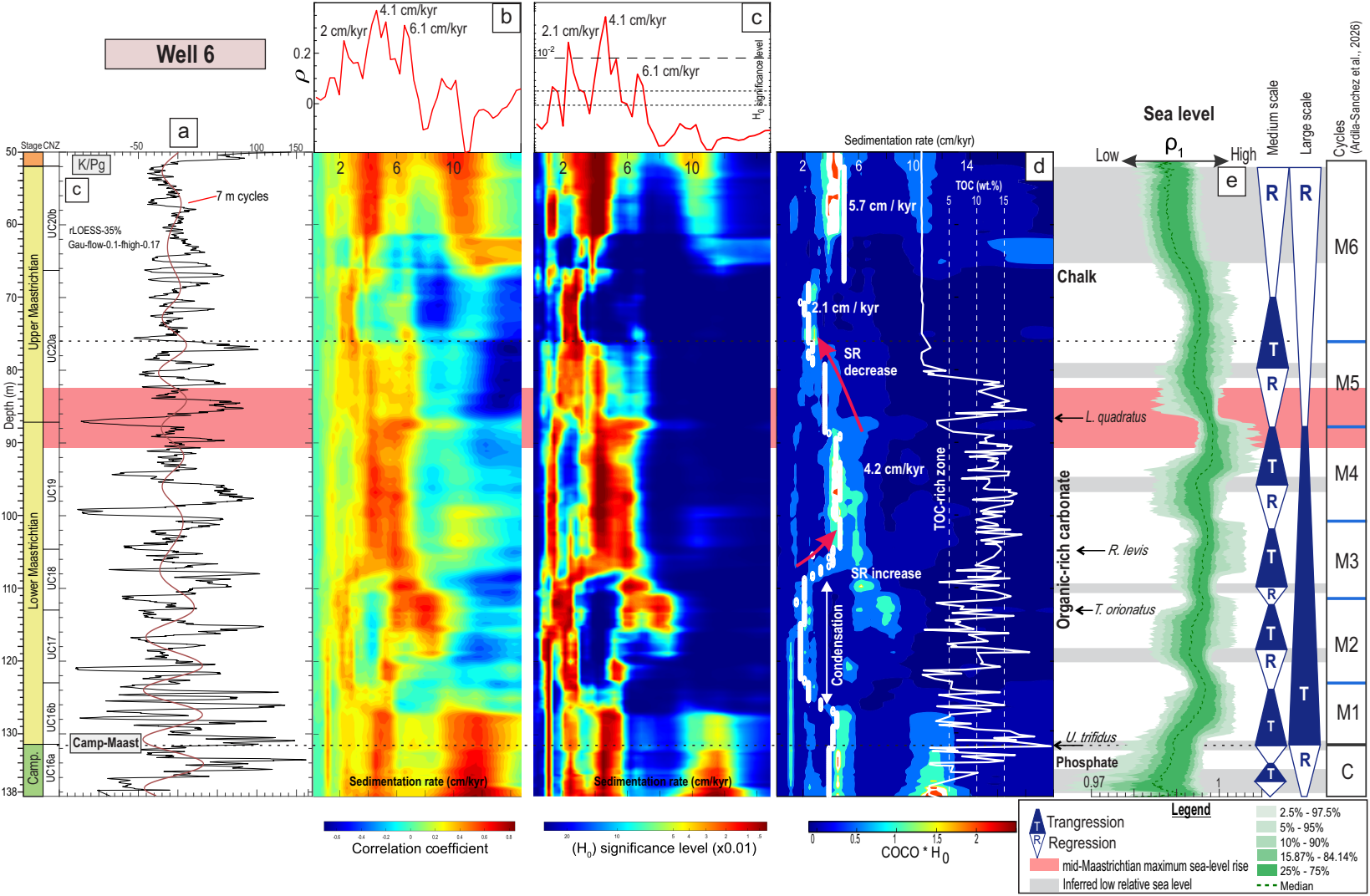
Robust AR(1) 99% — Robust AR(1) median — Robust AR(1) 90% — K/Pg: Cretaceous–Paleogene boundary — e: 100-kyr eccentricity — E: 405-kyr eccentricity — P: Precession

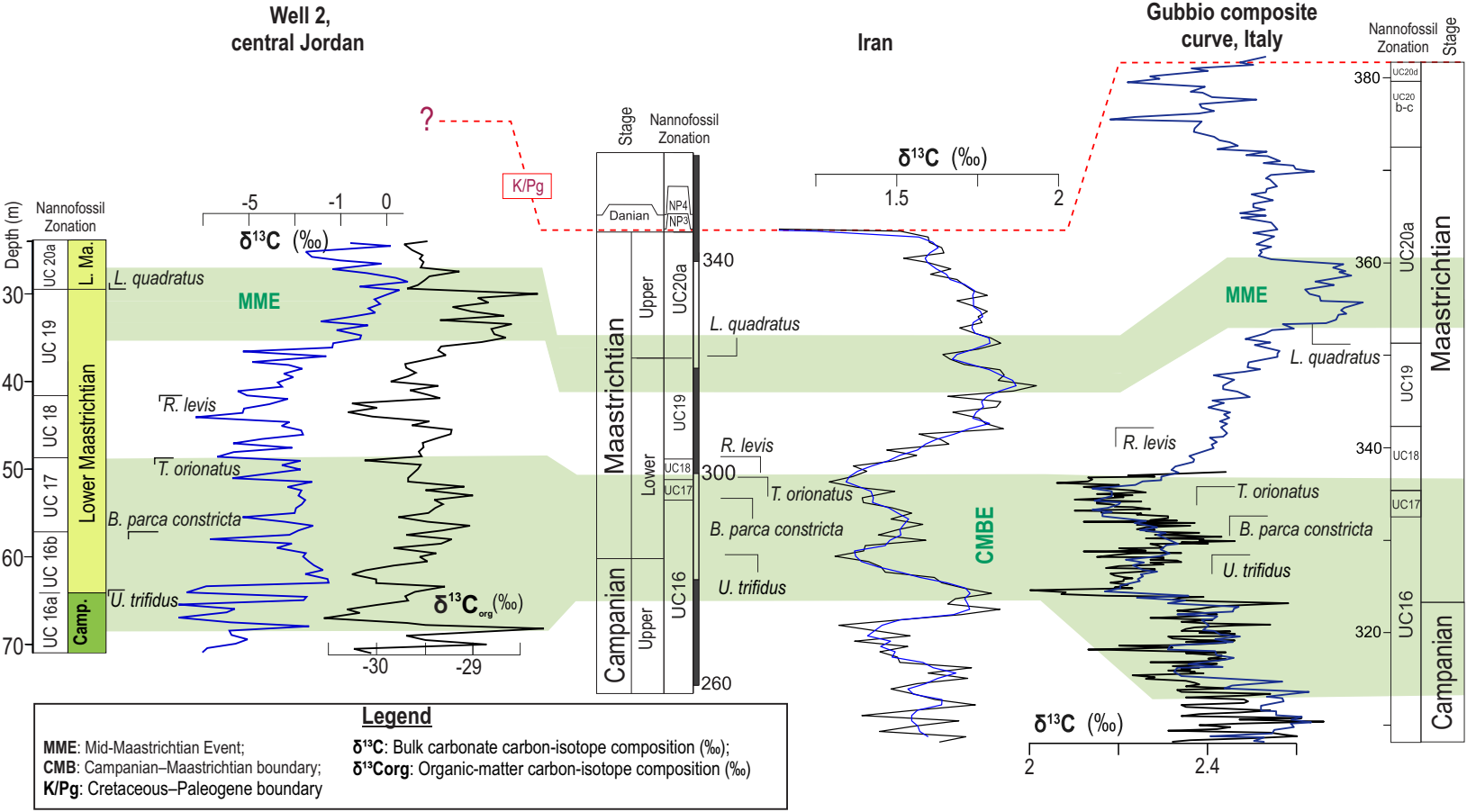
Robust AR(1) 95% — 20% median-smoothed — kyr: thousand years — AR(1): First-order autoregressive (red-noise) model — RLOESS – Robust locally estimated scatterplot smoothing



Legend

Robust AR(1) 99% — Robust AR(1) median — Robust AR(1) 90% - - Robust AR(1) 95% 20% median-smoothed kyr: thousand years e: 100-kyr eccentricity E: 405-kyr eccentricity P: Precession

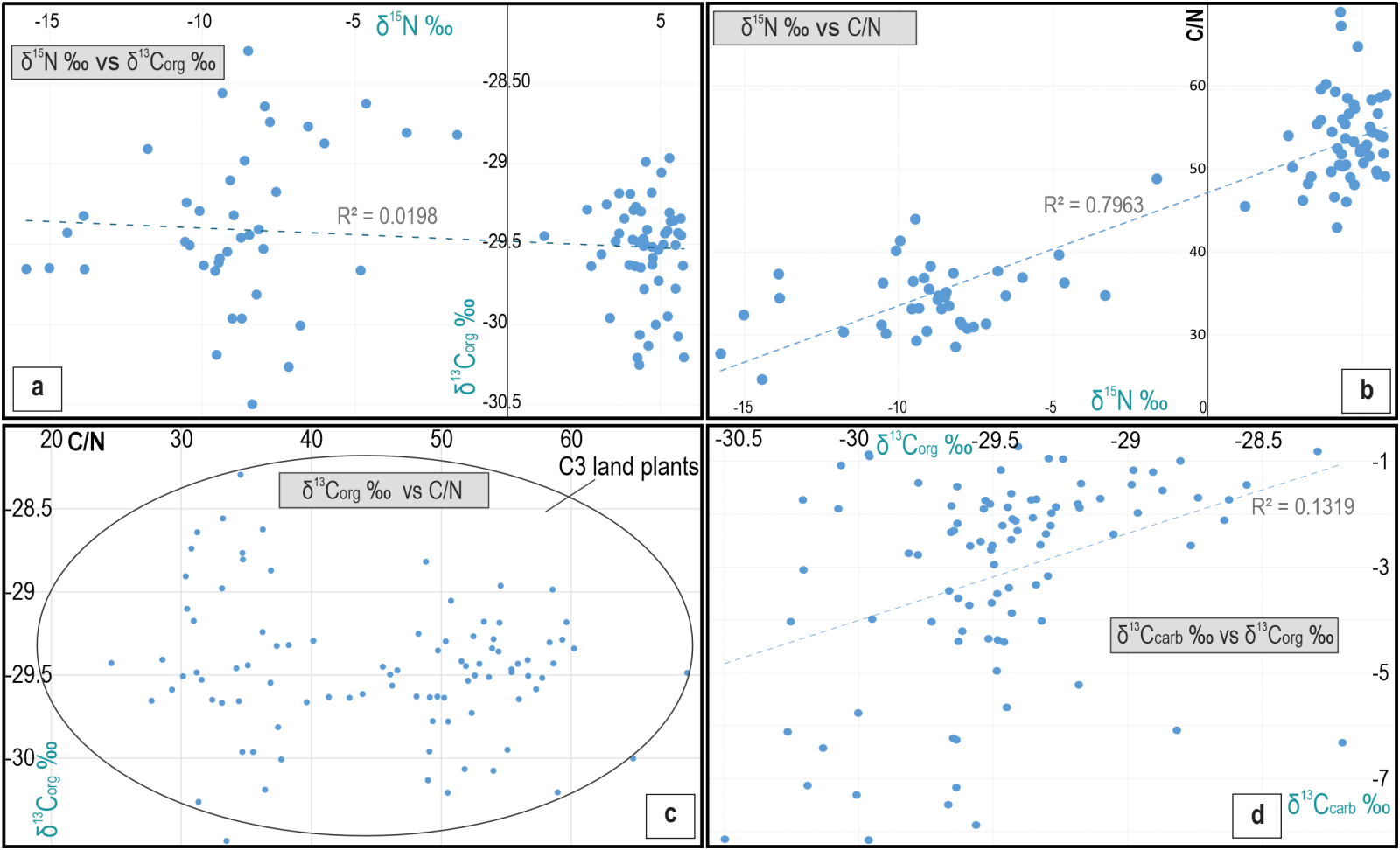

Well 6
a
b
c
d
e
2 cm/kyr
4.1 cm/kyr
6.1 cm/kyr
2.1 cm/kyr
10-2
H0 significance level
Stage CNZ
K/Pg
Camp-Maast
Upper Maastrichtian
Lower Maastrichtian
Camp.
UC20b
UC20a
UC19
UC18
UC17
UC16b
UC16a
Depth (m)
7 m cycles
rLOESS-35%
Gau-flow-0.1-fhigh-0.17
Sedimentation rate (cm/kyr)
Correlation coefficient
(H0) significance level (x0.01)
COCO * H0
5.7 cm / kyr
2.1 cm / kyr
SR decrease
4.2 cm/kyr
SR increase
Condensation
TOC-rich zone
TOC (wt.%)
Chalk
L. quadratus
Organic-rich carbonate
R. levis
T. orionatus
U. trifidus
Phosphate
0.97
Sea level
Low
High
Medium scale
Large scale
Cycles (Ardila-Sanchez et al., 2026)
M6
M5
M4
M3
M2
M1
C
Legend
Trangression
Regression
mid-Maastrichtian maximum sea-level rise
Inferred low relative sea level
2.5% - 97.5%
5% - 95%
10% - 90%
15.87% - 84.14%
25% - 75%
Median

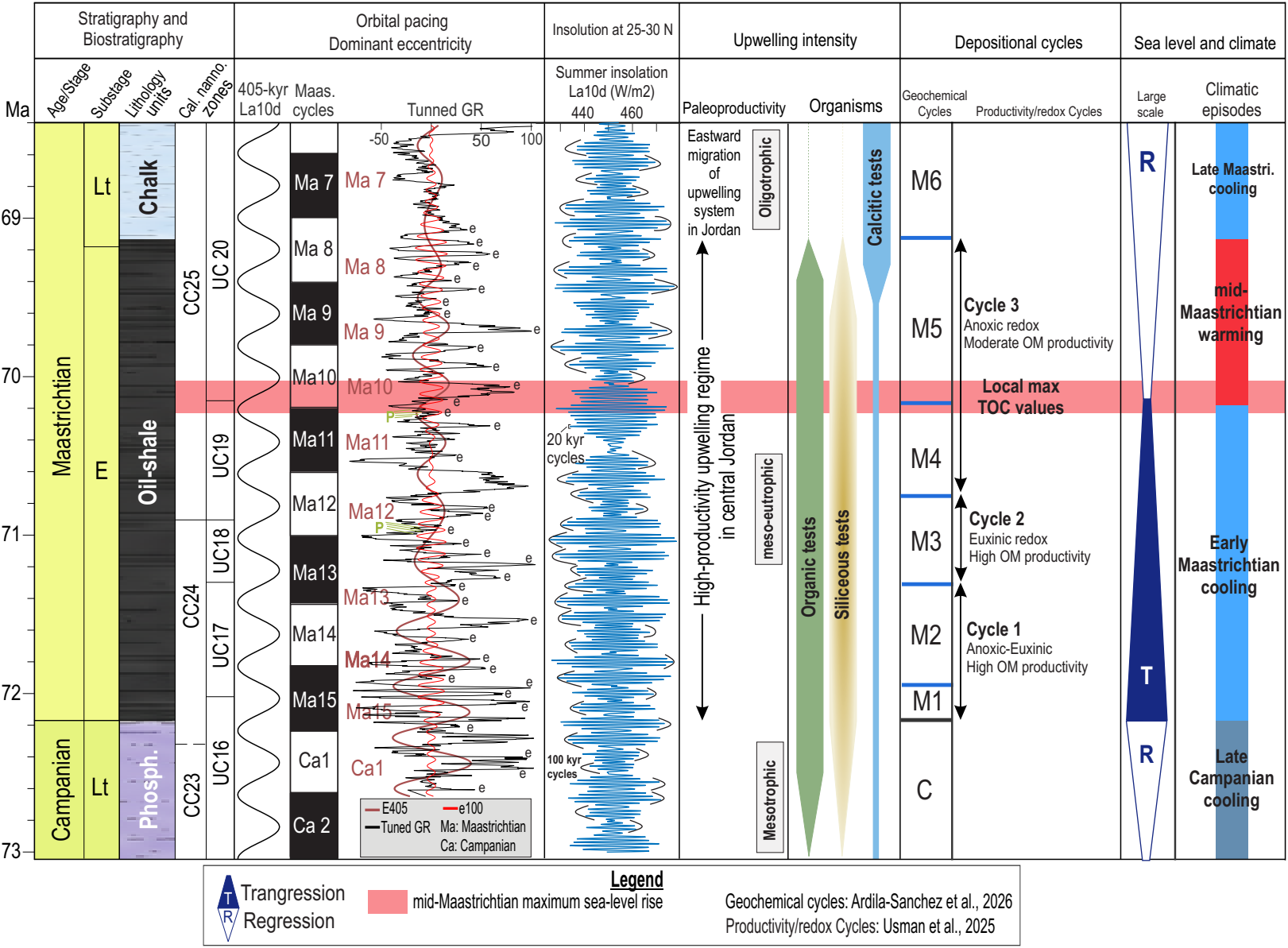


Legend

MME: Mid-Maastrichtian Event;
CMB: Campanian–Maastrichtian boundary;
K/Pg: Cretaceous–Paleogene boundary

δ13C: Bulk carbonate carbon-isotope composition (‰);
δ13Corg: Organic-matter carbon-isotope composition (‰)


δ15N ‰ vs δ13Corg ‰
δ15N ‰
δ13Corg ‰
R² = 0.0198
a
δ15N ‰ vs C/N
C/N
R² = 0.7963
δ15N ‰
b
δ13Corg ‰ vs C/N
C3 land plants
C/N
δ13Corg ‰
c
δ13Corg ‰
R² = 0.1319
δ13Ccarb ‰ vs δ13Corg ‰
δ13Ccarb ‰
d


Stratigraphy and Biostratigraphy
Orbital pacing
Dominant eccentricity
Insolation at 25-30 N
Upwelling intensity
Depositional cycles
Sea level and climate
Ma
Age/Stage
Substage
Lithology units
Cal. nanno. zones
405-kyr La10d
Maas. cycles
Tunned GR
Summer insolation La10d (W/m2)
Paleoproductivity
Organisms
Geochemical Cycles
Productivity/redox Cycles
Large scale
Climatic episodes
Maastrichtian
Campanian
Lt
E
Lt
Chalk
Oil-shale
Phosph.
CC25
CC24
CC23
UC 20
UC19
UC18
UC17
UC16
Ma 7
Ma 8
Ma 9
Ma10
Ma11
Ma12
Ma13
Ma14
Ma15
Ca1
Ca 2
-50
50
100
440
460
20 kyr cycles
100 kyr cycles
E405
Tuned GR
e100
Ma: Maastrichtian
Ca: Campanian
Eastward migration of upwelling system in Jordan
High-productivity upwelling regime in central Jordan
Oligotrophic
meso-eutrophic
Mesotrophic
Organic tests
Siliceous tests
Calcitic tests
M6
M5
M4
M3
M2
M1
C
Cycle 3
Anoxic redox
Moderate OM productivity
Local max TOC values
Cycle 2
Euxinic redox
High OM productivity
Cycle 1
Anoxic-Euxinic
High OM productivity
R
T
R
Late Maastri. cooling
mid-Maastrichtian warming
Early Maastrichtian cooling
Late Campanian cooling
69
70
71
72
73
Legend
Trangression
Regression
mid-Maastrichtian maximum sea-level rise
Geochemical cycles: Ardila-Sanchez et al., 2026
Productivity/redox Cycles: Usman et al., 2025